LA-UR-21-29559
Accepted Manuscript

Tribological behaviors of nanotwinned Al alloys

Zhang, Yifan
Niu, Tongjun
Sun, Tianyi
Richter, Nicholas
Li, Nan
Xue, Sichuang
Li, Qiang
Wang, Haiyan
Zhang, Xinghang

To be published in: Applied Surface Science

DOI to publisher's version: 10.1016/j.apsusc.2022.154108

Permalink to record:
http://permalink.lanl.gov/object/view?what=info:lanl-repo/lareport/LA-UR-21-29559

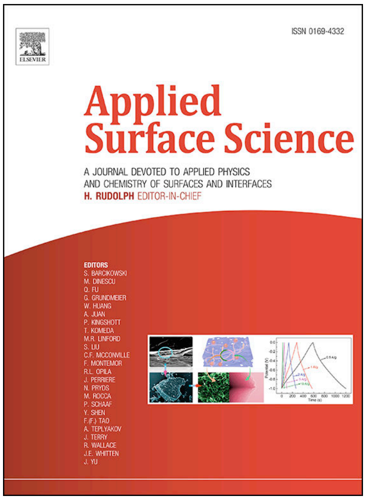

Full Length Article

Tribological behaviors of nanotwinned Al alloys

Yifan Zhang, Tongjun Niu, Nicholas A. Richter, Tianyi Sun, Nan Li, Haiyan Wang, Xinghang Zhang

PII: S0169-4332(22)01644-0
DOI: https://doi.org/10.1016/j.apsusc.2022.154108
Reference: APSUSC 154108

To appear in: *Applied Surface Science*

Received Date: 31 March 2022
Revised Date: 19 June 2022
Accepted Date: 27 June 2022

Please cite this article as: Y. Zhang, T. Niu, N.A. Richter, T. Sun, N. Li, H. Wang, X. Zhang, Tribological behaviors of nanotwinned Al alloys, *Applied Surface Science* (2022), doi: https://doi.org/10.1016/j.apsusc.2022.154108

Tribological behaviors of nanotwinned Al alloys

*Yifan Zhang** [a, b], *Tongjun Niu* [a], *Nicholas A. Richter* [a], *Tianyi Sun* [a], *Nan Li* [c], *Haiyan Wang* [a,d], *Xinghang Zhang** [a]

[a] *School of Materials Engineering, Purdue University, West Lafayette, IN 47907, USA*

[b] *Materials Science and Technology Division, Los Alamos National Laboratory, Los Alamos, NM 87545, USA*

[c] *Center for Integrated Nanotechnologies, Los Alamos National Laboratory, Los Alamos, USA*

[d] *School of Electrical and Computer Engineering, Purdue University, West Lafayette, IN 47907, USA*

Abstract

Wear-induced damages cause significant materials loss each year. Al alloys are widely used by industry but usually have low wear resistance. Here, we compare the tribological behaviors of ultrafine grained Al, a nanoprecipitate hardened Al 7075 alloy and nanotwinned Al–Ni alloys using the nanoscratch. The nanotwinned Al–Ni alloys exhibit lower coefficient of friction and much greater wear resistance than the Al and Al 7075 alloys. The enhanced wear properties of Al–Ni alloys arise from their high strength and the evolution of nanotwinned microstructures into gradient nanograins during wear. These findings on fundamental wear mechanisms in nanotwinned alloys may advance the discovery of wear-resistant metallic materials.

Key words: Tribological behavior; Nano scratch; Al alloys; Nanotwin.

*Corresponding author: Xinghang Zhang: xzhang98@purdue.edu; Yifan Zhang: yfzhang@lanl.gov;

1. Introduction

Wear and friction induced energy and material losses account for 23% of the world's total energy consumption [1]. Therefore, developing wear-resistant and low-friction materials is critical for reducing carbon emissions and environmental protection. Light-weight Al alloys are widely used for transportation applications because of their high–specific strength, good corrosion resistance [2], high thermal conductivity [3], and energy savings [4]. However, the wear resistance of most Al alloys is poor [5–8]. For instance, the specific wear rates of commercial Al alloys are several times higher than those of steels [5].

Tribological behaviors include the friction and wear responses of interacting surfaces [9]. A low coefficient of friction (COF) and high wear resistance are ideal for structural materials exposed to wear environments [10,11]. Nanoscratch is a well-developed nanomechanical testing method [12,13] to evaluate the nano and microscale tribological behaviors of materials. Compared with macroscale wear testing methods, nanoscratch is more versatile and precise and can be used to evaluate the wear properties, interfacial adhesion, and underlying wear mechanisms of various materials [14–16]. The loading mode (constant or ramping), scratch speed, indenter geometry, and penetration depth can be precisely controlled during nanoscratch. Noh *et al.* [17] proved that the wear properties of automotive coatings measured using the nanoscratch method correlated well with those from Amtec-Kistler car-wash tests. Prior studies have also shown strong correlations between both fretting and sliding wear with nanoscratch tests [14,15], indicating that nanoscratch testing is a reliable method to explore the wear and friction properties of Al alloys and other metallic materials.

Recently, nanoscratch has been used to investigate the wear behaviors of advanced metallic materials including metallic glass [18], metallic nano laminates [19,20], high entropy alloys [11] . Luo and Wang *et al* [19] investigated the wear behaviors of NbMoW/Ag nanolaminates and found that the introducing of Ag can greatly decrease the friction and remain the high hardness. By using nanoscratch tests, Jia *et al* [18] discovered that the surface oxidation generated the best anti-wear performance in Zr based metallic glass due to the weakened interfacial bonds. Most recently, Wang and Cai *et al* [20] studied the tribocorrosion behaviors of Al based multilayers by coupling the nanoscratch with corrosion tests and found the Al-Ti combination has the best tribocorrosion resistance. Ye *et al* [11] compared the friction and wear behaviors of TiZrHfNb HEAs and Nb alloys via nanoscratch and demonstrated that TiZrHfNb HEA had superior wear properties than tradition alloys.

The wear behaviors of Al under nanoscratch have also attracted extensive research interests recently. Shi and Szlufarska [5] investigated the wear behaviors and microstructure evolutions of nanocrystalline (NC) Al alloys with Zr solutes by using molecular dynamics simulations. The revealed that NC Al-Zr alloys have better wear resistance and smaller friction than NC Al in single scratch cycle due to suppressed GB activities. However, the trend was reversed in multi-cycle nanoscratch tests due to more strain hardening. In addition, there are a number of experimental efforts in understanding wear behaviors of Al and Al alloys via nanoscratch as well. Y. Wang *et al* [21] studied the wear behaviors of Al under dry, water and aqueous H_2O_2 conditions and observed the "stick-slip" phenomenon in H_2O_2 condition. Kim *et al* [22] and Huang *et al.* [23] have both investigated the wear properties of Al alloys using nanoscratch, without reporting the multiscale microstructure evolutions in Al alloys. Their studies show that abrasive wear is the dominant wear mechanism in Al alloys under nanoscratch. The mass transport of material is mainly accommodated by dislocation activities [8]. Additionally, prior studies [23,24] proved that wear debris forms easily in Al even at small normal loads, indicating a poor wear resistance of Al. The addition of second-phase inclusions, such as Al-Si/Ti precipitates [22], Pb particles [8], carbon nanotubes [25], Al_2O_3 [26] and Si [24] can improve the wear resistance of Al by increasing the density of dislocation barriers and promoting dislocation activities [8,23]. Unfortunately, the benefit of second-phase particles on wear resistance is limited by their dimensions and distribution and degrades significantly with increasing load due to the formation of cracks at the particle-matrix interfaces [8,23].

However, most of these experimental studies on Al merely focused on single type of Al alloy examined via one or two characterization techniques, such as scanning electron microscopy (SEM), scanning probe microscopy (SPM), or atomic force microscopy (AFM). Due to limit of spatial resolution and imaging mechanisms , SEM, AFM and SPM can only provide the surface morphological information of the scratch sites. The wear-induced micro and nanoscale microstructure evolutions beneath the scratch surface cannot be obtained from these SEM and SPM analyses. Consequently, wear mechanisms, wear-induced microstructural and crystal orientation evolutions are not well comprehended. Besides, there is a lack of comparative and comprehensive study on Al alloys with different microstructures. To resolve these issues, we adopted versatile characterization techniques to uncover multiscale microstructure evolutions in three different Al alloy samples.

Nanotwinned (NT) materials have high strength [27], outstanding thermal stability [28,29], and improved radiation tolerance [30]. However, their wear properties are less well understood. Yan and

Hodge *et al* [31] investigated the sliding wear behaviors of NT Cu alloys by using focused ion beam (FIB) imaging at low-mag SEM images. They found that NT Cu-Ni has best wear resistance. However, their study failed to illustrate how twin boundaries can evolve during sliding wear process due to the limit of their characterization techniques. Despite twinning is a common phenomenon, twinning in Al is rare because of its high stacking fault energy (142 mJ/m^2) and low detwinning energy barriers [32]. Recently, NT Al alloys with abundant incoherent twin boundaries (ITBs) and stacking faults (SFs) were fabricated by magnetron sputtering [33,34]. While NT Al alloys have shown high flow stress (1 GPa) and good deformability under compression, their tribological properties have not been investigated.

Here, we present the first in-depth study on the friction and wear behaviors of NT Al alloys via nanoscratch testing. As a comparison, the tribological behaviors of ultra-fine-grained (UFG) Al, Al7075 were also systematically studied. In addition, multiscale characterizations are performed to ensure a comprehensive and detailed interpretation of the wear-induced microstructure evolutions in different Al alloys. Our nanoscratch tests show that NT Al-Ni alloys exhibit better wear resistance compared with the UFG Al and Al 7075 alloys with nanoprecipitates. The outstanding wear resistance of NT Al is due to their high strength and good work hardening capability ensured by unique microstructure evolutions during scratch. This study unravels an interesting wear mechanism enabled by nanotwins and provides a fresh perspective on the design of wear–resistant metallic materials.

2. Experiments

NT Al–Ni alloys and pure Al films 1.6 μm in thickness were deposited on Si (111) substrates via magnetron sputtering at room temperature. Pure Al and Al-Ni films were deposited by using high-purity Al (99.99%) and Ni (99.99%) targets in the vacuum chamber of an AJA sputtering system. Prior to deposition, the chamber was evacuated to a base pressure of 8×10^{-9} torr. During the deposition, the Ar pressure was maintained at 2×10^{-3} torr. Substrates were rotated to promote film uniformity. After deposition, specimens were mounted onto PELCO Atomic Force Microscopy (AFM) discs using superglue for hardness and nanoscratch tests. Details regarding the deposition parameters can be found elsewhere [34]. The commercial Al 7075 T6 alloy was prepared by mechanical grinding via 800-grit SiC paper, polishing with 1μm and 0.3 μm diamond pastes, and vibratory polishing with 50 nm colloidal silica. Hardness, Young's modulus, and surface roughness of each sample were measured by using Bruker TI Premier Nanoindenter equipped with Berkovich tip. At least 150 indents with different penetration depths were conducted on each sample using the displacement control mode. Microstructure and chemical composition of each sample were examined by using transmission electron microscopy (TEM) on a Thermo Fisher Talos 200X analytical microscope equipped with the Super X energy–dispersive X–ray (EDX) detectors at 200 kV.

Nanoscratch tests were performed using a diamond conical tip on the Bruker TI Premier Nanoindenter. As shown in Fig. 1 (a), the radius of conical tip is 5.03 μm with a 60º apex angle. High-load nanoscratch tests were performed at constant normal applied load (*P*), ranging from 5 to 70 mN. The scratch speed and scratch length were 8.33 μm/s and 250 μm, respectively. At least 5 repeated scratch tests were conducted at different locations of each sample to ensure the data reliability. Before nanoscratch tests, the surface roughness was measured by SPM using a Berkovich tip inside the Bruker TI Premier Nanoindenter. Post-scratch SPM scans were used to probe the tomography and residual depth along the scratch sites.

Samples after scratch were further examined using the Thermo Fisher Quanta 3D FEG scanning electron microscope. TEM samples were cut and lifted out from scratch sites of Al 7075, Al-3.2Ni and Al-7.8 Ni using focused ion beam (FIB) and the OMNI probe. Lift-out TEM lamellae were thinned down to 400 nm by using beam voltage of 30 kV and beam current of 0.3 nA. In the following step, the 400nm-thick TEM lamellae were thinned down to 150 nm by using 5 kV acceleration voltage and 48 pA beam current. The final polishing was finished using a beam voltage of 2 kV with 27pA beam current to minimize the ion damage. Post-mortem TEM analyses were performed to check the microstructure and chemical composition after scratch. Crystal orientation examination was conducted on the NanoMegas ASTAR automated crystal orientation mapping system installed on the Thermo Fisher TALOS 200X microscope based on the procession electron beam diffraction technique [35]. The step size used for ASTAR analyses was 3 nm. Datasets collected by ASTAR were analyzed using the OIM software. To ensure the reliability of the data, only grain confidence index (CI) standardization and neighbor CI correlation (NCIC) were performed to clean the ASTAR datasets.

3. Results

3.1 Pre–scratch microstructures and mechanical properties

The microstructural analysis and mechanical properties for the Al7075 and NT Al–Ni alloys are summarized in Fig. 1 and Table 1. The Al 7075 alloy has coarse grains with an average grain size of ~ 10 μm. Bright-field (BF) and dark-field (DF) TEM micrographs and an EDS map Fig. 1 (b–d) reveal high-density of Al_2Cu and $MgZn_2$ precipitates, ranging in size from tens to several hundred nanometers, distributed throughout the Al 7075 sample. Cross-section TEM micrographs show that the Al-3.2Ni and Al-7.8 Ni alloys are composed of columnar grains with average column sizes of 53 and 8 nm, respectively (Fig. 1 (e, and i)). An ASTAR inverse pole figure (IPF) map shows polycrystalline grains in the Al-3.2Ni alloy, and a pole figure map (Fig. 1(h)) prominently shows both matrix and twin diffraction spots. The NT Al-Ni alloys possess 9R phases as presented using HRTEM in Fig. 1(j). The IPF for Al-7.8Ni in Fig. 1(k) demonstrates strong (111) texture along the growth direction, and the grain boundary map in Fig. 1(l) reveals columnar grain boundaries containing abundant twin boundaries. As listed in Table 1, the grain size of NT Al–Ni alloys decreases from 53 to 8 nm with increasing Ni composition from 3.2 to 7.8 at.%. The UFG Al (not shown here) has an average grain size of ~500 nm.

Other physical properties, including surface roughness, hardness (*H*), Young's modulus (*E*), and sample thickness are also summarized in Table 1. The hardness of NT Al–Ni alloys varies between 5.1 and 6.4 GPa, much greater than that of pure Al (0.78 GPa) and Al 7075 (2.1 GPa). The Young's modulus (E) is derived from the measured reduced modulus (E_r) from nanoindentation by using the following formula [36]:

$$E = \frac{1 - v^2}{\frac{1}{E_r} + \frac{{v_i}^2 - 1}{E_i}} \qquad (1),$$

where, v and v_i are the Poisson's ratio of tested Al samples (0.35) and the diamond indenter (0.2), respectively, and E_i is the modulus of the diamond indenter (E_i =1050 GPa). As shown in Table 1, the UFG Al and Al 7075 have a Young's modulus of 70 GPa. In comparison, the Young's modulus of NT Al-Ni alloys increases to 105 – 110 GPa.

3.2 Nanoscratch and friction behaviors

The total normal displacement (elastic and plastic), or the penetration depth (*h*), during nanoscratch testing was recorded and plotted against the lateral displacement (Fig. 2, Table S1). Fig. 4 (a) displays that the normal displacements increase with the normal applied load (*P*). At the same applied load, UFG Al and Al 7075 have drastically larger normal displacements than that of the NT Al-Ni alloys. Fig. 2 shows that the displacement curves become rougher at larger normal applied loads ($P >$ 30 mN). The normal displacement curves of Al and Al 7075 vary much more than those of the NT Al–Ni alloys.

The coefficient of friction (COF) of each sample is compared as a function of the lateral displacement (Fig. 3) and the normal applied load (Fig. 4(b), Table 2). When $P \leq 10$mN, the COF of Al 7075 (0.25) is comparable to that of NT Al-Ni alloys (0.2 – 0.25), while the COF of pure Al is 0.49 when $P = 5$ mN. As P increases, differences in the COF between Al 7075 and NT Al-Ni alloys become more pronounced. The COF of Al 7075 grows monotonically with increasing normal load, reaching a peak of 0.70 when P = 70 mN, while the COF for most NT Al-Ni alloys increase moderately with applied load to 0.37 – 0.39. Additionally, as shown in Fig. 3, the COFs of NT Al–Ni alloys remain more stable than Al 7075 within the entire lateral displacement range.

3.3 Post–scratch SPM analysis and wear behaviors

Scratch sites were examined post-scratch using SPM to measure the residual penetration depth and scratch topography. Fig. S2 shows the three-dimensional (3D) topography of Al-3.2Ni scratches under different applied loads (5 – 70 mN). Pile-up of materials is evident along scratch grooves. Fig. 4 (c-d) contains representative cross sectional profiles of scratch sites under different loading conditions. It should be noted that the X axis unit is μm, while the Y axis is plotted using nm in Fig. 4 (c-d). As applied load increases, the depth and width of scratch grooves increase accordingly. Under the same applied load of 10 mN, NT Al–Ni alloys have much shallower and narrower scratch grooves than those of UFG Al and Al 7075 (Fig. 4(c)). The scratch groove depth is equal to the residual (plastic) normal displacement (h_R) of the indenter tip. This data is compiled in Fig. S1 (a) using dashed lines, whereas the total normal displacement is plotted using solid lines. The numerical values of the total normal displacement and the residual normal displacement are summarized in Table S1 and Table S2.

As shown in the Fig. 5 (a), the residual scratch depth (h_R) can be used to calculate the contact radius and cross–section wear area (shown as green shadows). When $h_R < h_{max}$ (2.52 μm), the residual contact radius (a_R) of the scratch grooves can be estimated as:

$$a_R = \sqrt{2Rh_R - {h_R}^2} \qquad (2),$$

where R is the radius of the diamond tip. Then the cross–section wear area (A_w) is calculated as:

$$A_W = 2\mathrm{R}^2 \sin^{-1}\left(\frac{a_R}{R}\right) - (R - h_R)a_R \qquad (3).$$

The wear rate (W_R) is defined as the removed volume per unit distance and per unit normal applied load, and can be calculated as:

$$W_R = \frac{V}{xP} = \frac{A_W}{P} \qquad (4),$$

where, V is the is the wear volume, x is scratch distance, P is the normal applied load. The calculated wear rates are summarized in Table 3 and plotted against the normal applied load in Fig. 5(b). It is shown that the wear rates of NT Al–Ni alloys are several times lower than those of UFG Al and Al 7075. At an applied load of 30 mN, the wear rates of Al, Al 7075, and Al–3.2Ni are 163.6×10^{-3}, 72.1×10^{-3} and 17.0×10^{-3} $mm^3/(N\cdot m)$ respectively.

Based on the Archard equation [37], the wear volume (V) induced by nanoscratch testing can be expressed as:

$$V = \frac{KP}{H}x \qquad (5),$$

where K is the wear coefficient, H is the hardness, x is the scratch distance. Combined Eq. 4 and 5, we arrive:

$$P = \frac{H}{K} \cdot \frac{V}{x} = \frac{H}{K}A_W \quad , \quad R_W = \frac{H}{K} \qquad (6),$$

where the R_w is the wear resistance [38]. If we plot the normal applied load (P) against the wear area (A_w), the wear resistance (R_w) can be derived from the slope of the resulting P–A_w plots [11,15] as shown in Fig. 5(c). Interestingly, we found the P–A_w curves possess two slightly different slopes at different load ranges. The slope of the NT Al-Ni alloys and Al 7075 P–A_w curves is greater when $P < 30$ mN. Hence, we performed curve fitting for different load ranges to account for this phenomenon and the results are summarized in Table 4 and Fig. S1 (b–c). When $5 \le P \le 30$ mN, the wear resistance of NT Al–Ni alloys is 51 – 56 GPa, more than 11 times higher than UFG Al (4.4 GPa), and 4 times higher than that of Al 7075 (12.1 GPa).The Al–4.5Ni exhibits the highest wear resistance of 56.1 GPa when $P \le 30$ mN. As $P \ge 30$ mN, the wear resistance of Al 7075 and NT Al–Ni alloys drops to 4.7 GPa and 24 – 35 GPa, respectively. The overall wear resistances of samples are calculated on the basis of the linear fit of P–A_w plots in the full load range of 5-70 mN, which are presented in Fig. 5(d) and Table 4. The wear resistances of Al-Ni alloys are 30-39 GPa in the load range 5-70 mN, which are more than 5 times higher than that of Al7075 (~6 GPa).

3.4 SEM analyses on scratch sites

Post-scratch SEM analysis was performed to characterize the scratch trace morphologies on Al 7075, Al–3.2Ni and Al–7.8Ni under different loads. The volume of cutting chips increases at higher applied load. Cutting chips appear on UFG Al at 5 mN (Fig. S3 (a_1)). When P ≥ 30 mN, the UFG Al sample delaminated, leading to the exposure of the Si substrate (Fig. S3(c_1–d_2)). As shown in Fig. 6 (a), certain volume of material was removed from Al 7075 as cutting chips at the end of scratches when P ≥ 30 mN. In comparison, scratch sites on NT Al–Ni alloys were free of cutting chips and wear debris. When P ≤ 10 mN, the Al 7075 scratch sites have smooth groove edges with material pileups and shear traces and a small cutting chip at the end of the scratch groove, as shown in high magnification SEM micrographs in Fig. 6 (d–e). Meanwhile, some shear serrations were detected at the edge of scratch grooves (Fig. 6(f)). Higher applied loads (P ≥ 50 mN) led to periodical shear bands at the edge of scratch grooves. In comparison, Fig. 6 (i–k) illustrate that Al-3.2Ni forms smooth scratch grooves with pileups when P ≤ 30 mN. Shear serrations form along the scratch groove edge on the Al-3.2Ni and Al-7.8 Ni at the load threshold of 50 and 30 mN, respectively as shown in Fig. 6(l) and Fig. 6(p).

3.5 Scratch induced evolution of microstructures

Fig. 7-8 show the evolution of microstructure and crystal orientation of Al7075 after nanoscratch conducted with *P* = 30 mN. The BF cross-section TEM (XTEM) image in Fig. 5 (a) contains an overview of the scratch site. Some precipitates aggregate near the scratch surface, and material pile-ups and shear serrations occurred near the edge of scratches. Several dislocation bands underneath the scratch surface are highlighted by yellow arrows. These dislocation bands identified in the BF TEM micrograph in Fig. 5 (b) and the BF STEM images in Fig. 5 (c–d) have a dislocation density of $2.2\times10^{14}/m^2$. The average dislocation density in the scratch zone is $5\times10^{13}/m^2$, greater than that of the as–received sample ($1\times10^{13}/m^2$). Noticeably, the shape of these dislocation bands is similar to the scratch groove. Scratch zones in this study are defined as regions under the scratch surface with evident changes in microstructures and crystal orientations induced by scratch. The width of scratch zone is similar to the width of scratch groove and the depth of scratch zone is comparable to the penetration depth. Additionally, the boundary between scratch zone/none-scratch zone is akin to the shape of scratch surface.

Fig. 8 presents the ASTAR analyses of the scratch sites in Al 7075. The phase map in Fig. 8 (a) displays these scattered $MgZn_2$ (green) and Al_2Cu (blue) second phases in Al matrix. The IPF map in Fig. 8 (b) shows the development of an orientation gradient from the scratch surface to the interior of the specimen. Away from the scratch surface, the Al matrix has a <110> orientation along the A_3 axis (scratch direction), whereas the specimen is <111> orientation dominated near the surface of the scratch site. Line-scan analysis (Fig. 8 (c)) identifies small point-to-point (< 3 degrees) and large (40 – 60 degrees) point-to-origin orientation changes along scanning paths 1 – 3, confirming the gradual orientation evolution from the specimen surface to the matrix after the scratch. Additionally, there very few deformation-induced new grains of Al grains.(Fig. 8 (d)). The KAM map (Fig. 8 (e)) reveals the accumulation of a high-density of GNDs, manifested as local misorientation variations.

The post-scratch (P = 70 mN) microstructures and orientation information for the NT Al-Ni alloys were characterized using TEM and ASTAR. It is identified that the surface profiles of the scratch grooves, as outlined by black dash lines (Fig. 9(a), 10(a)), are identical to the shape of the tip for both NT Al–3.2Ni and Al–7.8Ni alloys. The measured radii of the scratch grooves (R_{sg}) were 5.0 µm, nearly the same as that of the diamond tip (R = 5.03 µm). The residual film thicknesses of Al–3.2Ni and Al–7.8Ni were 920 and 1030 nm, respectively, indicating a residual penetration depth of 680 and 570 nm, consistent with results from SPM analyses (Table. S2). Hence, our calculations of wear volumes based on SPM analysis are reliable.

The scratch sites of NT Al-Ni alloys can be divided into four zones separated by blue dashed lines in Fig. 9 (a) and Fig. 10(a), corresponding to the less-deformed (zone I), transition (zone II), deformed center (zone III), and surface nanograined zones (zone IV). Zone I has a high density of twins and stacking faults, with the SAD pattern collected in zone I in Al–7.8Ni supporting the NT microstructure (Fig. 10 (a)). As shown in Fig. S5 (a), zone I in Al–3.2 Ni is composed of highly faulted columnar grains. In Zone II, grain rotation, detwinning, and defaulting processes took place. As shown in Fig. 9 (b–c), columnar grains reoriented to align with the scratch surface, contributing to the formation of zone IV. Distorted 9R phases coexist with nanograins in Zone II (Fig. 10(d, e)). The existence of 9R phase can also be confirmed using the inserted fast Fourier transform (FFT) patterns revealing twinned diffraction patterns and the diffraction spots of the 1/3{111} planes.

Zone III and part of zone IV are located directly underneath the indenter, and they consist of nanograins. Interestingly, this region has a grain size gradient as a function of distance from scratch surface as shown in Fig. 9 (d) and Fig. 10 (c). The surface nanograin regions (zone IV) in NT Al-Ni alloys are composed of extremely fine nanograins with some residual 9R phases (Fig. 10 (b, d)). It is worth mentioning that segregation of Ni solutes was absent at scratch sites of NT Al-Ni alloys (Fig. S5).

ASTAR analysis clearly illustrates the post-scratch evolution of grain orientation and GBs of the Al-Ni alloys. Inverse pole figure (IPF) maps prove that zone I-IV have distinct orientations along the A_3 axis (scratch direction) and A_1 axis (growth direction). As shown in Fig. 11-12 (a, b), Al-3.2Ni and Al-7.8Ni in zone I have (111) and (110) textures along the A_1 and A_3 axes, respectively. Significant grain rotation was observed in both zone II and zone III. Furthermore, Fig. 11(b) shows zone IV of Al-3.2Ni has (110) textured equiaxed nanograins along the A_1 axis (growth direction), in drastic contrast to the (111) textured columnar grains in the matrix (zone I). Zone IV in Al-3.2Ni has strong (112) texture along the A_3 axis (zone axis), distinct from the other zones (Fig. 11(d)). Scratch induced grain rotation was also detected in the NT Al–7.8Ni (Fig. 12 (a, b), and Fig. S7). Pole figure analysis was also performed on different zones of the scratch sites (Fig. 11 (f), Fig. 12 (e), where the two sets of diffraction spots correspond to the matrix and twin orientations in Zone I. The removal of these twin spots in zones II-IV indicates that detwinning and grain rotation were induced during nanoscratch testing.

Fig. 11 (c) and Fig. 12 (c) show the distribution of LAGBs, HAGBs and ITBs in NT Al-Ni alloys. As shown in Fig. 12 (c), we divided the ITBs into three categories, including the less deformed vertical ITBs (circled by red dash line), the distorted and entangled ITBs (white dash line), and the residual shattered ITBs (green dash line). The ITB fraction in Al-7.8Ni decreases from zone I (0.23) to zone IV (0.08), confirming scratch induced detwinning. As shown in Fig. 11(e) and Fig. 12 (d), the LAGB fraction in both NT Al-Ni alloys dropped monotonically from zone I to zone IV, while the HAGB fraction increased sharply in NT Al-3.2Ni and NT Al-7.8Ni alloys.

4. Discussion

4.1 Microstructure evolution mechanisms

The microstructural evolution of UFG Al, Al 7075 alloys and NT Al-Ni alloys are drastically different after scratch tests. As shown in Fig. 7, several dislocation bands reside beneath the scratch surface in the Al7075 alloys. The accumulation of these GNDs identified in the KAM map in Fig. 8(e) caused a gradual crystal orientation change (Fig. 8 (c)). We infer that these dislocations are likely to nucleate from the scratch surface, propagate downwards, and assemble themselves into dislocation walls via cross slip as shown schematically in Fig. 14 (b). It should be noticed that microstructure evolution mechanisms as depicted in Fig. 14 are suitable for low-speed nano scratch tests. Alhafez *et al* [39] investigated the plastic zone induced by nanoscratch testing in Al, Cu, Ti *etc*. They reported that dislocations would nucleate from the scratch surface and immediately form networks via dislocation reactions and interactions upon scratch. The nucleation of dislocations from the scratch surface has also been observed by Li *et al* [40] and Shi *et al* [5] in their MD simulation studies. The accumulation of these GNDs is characteristic of the incipient stage of continuous dynamic recrystallization (cDRX) [41] in Al. These dislocation walls caused an increase in dislocation density of 4×10^{13} m^{-2}. Based on the Taylor equation [42], the hardness increase caused by dislocations is ~ 80 MPa. However, this limited strain hardening brought by the increase in dislocations may not be sufficient to resist scratch damages [43] and the plastic strains generated by these dislocation walls are insufficient to accommodate the deformation at higher applied loads. Thus, cutting chips were generated on the scratch surface of Al 7075 when $P \geq 30$ mN.

In contrast, NT Al–Ni alloys have unique deformation mechanisms and microstructure evolution under nanoscratch. As shown in Fig. 9-10 and Fig. 14(c), the columnar grains in the transition zone II bend during scratch. Column bending facilitated by grain rotation can increase the deformability and accommodate the mass transfer of materials along scratch grooves. Interestingly, NT columnar grains beneath the indenter evolve into equiaxed nanograins with both grain size and orientation gradients. The grain size distributions before and after the scratch are plotted as a function of the distance from the surface (Fig. 13 (a-b)). The grain sizes of the as-deposited Al-3.2Ni and Al-7.8Ni alloys decrease from the film surface to the substrate. In comparison, grain sizes of the scratched Al-3.2Ni and Al-7.8 Ni alloys developed a "peak". For the scratched Al-3.2Ni, the grain size started from 13 nm in the top 100 nm region on the surface (zone IV), increased to a peak of 81 nm at depth of 500 – 600 nm, and decreased to 26 nm near the substrate. Similarly, the top 50 nm zone IV near the scratch surface of Al-7.8 Ni had a grain size of 7 nm, and the grain size reached a maximum of 30 nm at the depth of 400 nm.

The formation of the gradient nanograins in NT Al alloys is a novel phenomenon and may be facilitated by TB dominated deformation mechanisms. Scratch-induced grain refinement in NT Al alloys can be classified as discontinuous dynamic recrystallization (dDRX) [44]. During the scratch test, NT columns can evolve into nanograins through detwinning and ITB migration via the collective glide of Shockley partials [45]. As shown in Fig. 12 (c), less deformed vertical ITBs gradually become distorted and evolve into HAGBs. Similarly, the dissociation of LAGBs and defaulting of SFs via the glide of partial dislocations may also contribute to the formation of nanograins. Because of this detwinning and defaulting, the nanograin regions contain fewer stacking faults compared with the less-deformed region

(Fig. 9 (e)). The statistics presented in Fig. 11 (e) and Fig. 12 (d) further support our assumption regarding the evolution of LAGBs and ITBs into HAGBs.

The stress/strain distribution is another factor contributing to the formation of gradient microstructure in NT Al–Ni alloys. The stress/strain levels induced by scratch testing decay from the surface to the interior of the sample. Moreover, both simulation and numerical calculations have proven that shear stress/strain dominates at the scratch surface, whereas normal stress/strain might be larger in the sub-surface region due to exponential decay of shear stress/strain [11,46,47]. Therefore, we assume that the shear–dominated severe plastic deformation on the surface is more likely to induce grain refinement through the aforementioned mechanisms, while the normal–stress–dominated and less severe deformation in the sub–surface region might cause grain coarsening in NT Al–Ni alloys [11,46,47].

4.2 Low COFs in NT Al alloys

NT Al–Ni alloys exhibit much lower COFs than their Al alloy counterparts (Table 5). Based on the friction law proposed by Amontons and Coulomb [48], the relationship between the normal applied force (F_N) and the tangent friction force (Ft) can be described as: $F_N = \mu F_t$, where μ is the coefficient of friction (COF). Bowden and Tabor proposed [49] that the macroscopic friction force should arise from two processes, including the adhesion between contact solids and the deformation of solids. The adhesion depends on physical properties like the interfacial shear strength of the contact interfaces, while the deformation process is correlated with the mechanical properties of contact pairs [50]. If we assume that adhesion and ploughing are two independent processes, then the COF (μ) is equal to the sum of the adhesion component (μ_{adh}) and the deformation component (μ_{def}).

The adhesion force between the tip and sample surfaces constitutes part of the friction force. Prior studies [11,51] have shown that the μ_{adh} decreases with increasing applied load and can be negligible when the applied load cause significant plastic deformation. Both experiments and simulations have also shown that the friction force is dominated by deformation rather than adhesion [50,51]. Therefore, the friction coefficients during the nanoscratch in the current study mostly originate from the deformation component (μ_{def}).

Deformation mechanisms during nanoscratch testing include ploughing, cutting and cracking, *etc.* Ploughing is assumed to be the dominant wear mechanism in ductile materials [5,52,53]. Studies show that the ploughing coefficient of friction (μ_{pl}) is governed by factors like the tip geometry, tip apex angle, penetration depth, and elastic recovery rate [50,53]. Goddard and Wilman proposed a model to calculate the ploughing COF for a spherical tip, and a conical tip with spherical extremity [9]:

$$\mu_{pl} = \frac{2}{\pi {a_i}^2}\left(R^2 \sin^{-1}\frac{a_i}{R} - a_i\sqrt{R^2 - {a_i}^2}\right) \quad (7),$$

where, a_i is the contact radius during scratch test, R is the radius of the tip. Eq. 7 indicates that the μ_{pl} should escalate with increasing penetration depth (h) when h $\ll R$, and reach a plateau when the penetration depth is comparable to the tip radius.

NT Al–Ni alloys have significantly smaller and more stable COFs than Al 7075 and UFG Al. Table 5 summarizes the COFs of Al alloys measured using different methods [8,21,22,54–59]. The ploughing model in Eq. 7 suggests that the low COFs of NT Al–Ni alloys may arise from their reduced normal penetration depth. However, our study shows that NT Al–Ni alloys have much lower COFs than those of UFG Al and Al 7075 alloys at similar penetration depths (as shown in Fig. 4(a-b)).

Cutting is another fundamental wear mechanism in the scratch process [60] and can remove a large amount of material from the sample, leading to the formation cutting chips [61]. The extra energy needed to remove materials and form new surfaces on cutting chips can increase the COF. For instance, the activation of the cutting mechanism when P = 30 mN causes a significant increase in the COF, rising from 0.27 to 0.45 for the Al 7075 alloy. SEM analyses show cutting chips formed in the UFG Al ($P \geq 5$ mN), and Al 7075 ($P \geq 30$ mN), but no cutting chips were present on the NT Al–Ni alloys, consistent with the low COF of NT Al–Ni alloys.

The development of scratch induced gradient nanograins may contribute to the low COF of NT Al–Ni alloys. These gradient nanograins evolve from NT columnar structures of Al-Ni alloys. Studies [62,63] have shown that gradient nanograins in Ti and Cu could reduce the COF during sliding. It has also been shown that gradient nanograins can increase the stability of the scratch surface and suppress surface roughing, delamination and cutting [64]. These findings support that the low COF of NT Al–Ni alloys arises from the unique gradient microstructure formation and the high strength of NT Al alloys.

4.3 Wear mechanisms

Several wear mechanisms are known to operate during the nanoscratch process, depending on the extent of surface damage or material loss. The ploughing mechanism, through which the sliding tip can displace material and result in material pileups as shown in Fig. 6(e), does not induce weight loss, and thus is considered as a mild wear mechanism [60]. In contrast, the cutting-chip mechanism involves the fracture of displaced materials in the form of wear debris [65], and is a severe wear mechanism that causes significant weight loss.

We discovered an interesting wear mechanism operating in NT Al alloys, *i.e.*, micro shearing. As shown in Fig. 6, periodical shear serrations or shear bands form along scratch grooves. Ghosh *et al.* [66] investigated the stress distribution using numerical calculations and found a maximum in shear stress ahead of the scratch tip whereas there is a maximum tensile stress behind the tip. The combined effects of shear and subsequent tensile stress might lead to the rupture of sample surface and pileups. The extent of damage induced by micro shearing lies between the ploughing and cutting mechanism.

In general, multiple wear mechanisms can coexist during scratch. Table S3 summarizes the wear mechanism of each sample under different loads. Ploughing and cutting ($p + c$) are the dominant wear mechanisms in UFG Al. When $P > 10$ mN, the wear mechanism of Al 7075 changes from ploughing to a combination of ploughing, shearing, and cutting ($p + s + c$). In comparison, NT Al–Ni alloys had ploughing at low loads ($P \leq 30$ mN) and ploughing plus shearing ($p + s$) at the higher applied loads. Cutting was absent in all NT Al–Ni alloys tested using conditions explored in this study. As a result, NT Al-Ni alloys have shown prominently improved wear resistance compared to the UFG Al and Al7075 alloys.

Overall, both extrinsic and intrinsic factors influence the activation of different wear mechanisms. Extrinsic factors include the loading condition, attack angle, tip geometry, and penetration depth *etc.* [65]. Hokkirigawa *et al.* [60] proved that a greater penetration depth can trigger severe wear mechanisms, like cutting. The wear mechanism of Al7075 evolves from ploughing to cutting with increasing penetration depth, in agreement with general perception. Intrinsic factors, such as microstructure and deformation capability of materials, and corresponding deformation mechanisms can also affect the operating wear mechanisms.

Zum Gahr *et al.* [61,67] described the severity of the abrasive wear f_{ab} by:

$$f_{ab} = 1 - \left(\frac{\varphi_{lim}}{\varphi_e}\right)^{2/\beta} ,$$

$$\beta = \left(\frac{H_{def}}{H_0}\right)^{1/3} \qquad (8),$$

where, φ_{lim} is the deformability of the sample and φ_e is the effective deformation on the scratch surface. β is a factor describing the work hardening behavior and can be calculated using the hardness of the severely deformed wear surface (or debris) (H_{def}) and the undeformed material (H_0). A higher f_{ab} indicates greater material loss and more severe wear damages.

Therefore, better deformability can induce a smaller f_{ab}. However, the deformability of materials highly depends on the deformation modes and loading conditions. The deformability of materials under tension and cold rolling does not necessarily assure a good wear resistance under nanoscratch. During scratch tests, the effective deformation on the surface can easily exceed the plastic deformability of the material ($\frac{\varphi_{lim}}{\varphi_e} < 1$), leading to significant wear damages on the sample surface. A high work hardening capability can alleviate the wear damage and give rise to a small f_{ab}. Using MD simulations, Li *et al.* [40] also proved that a higher work hardening rate can inhibit the formation of cutting chips in nanocrystalline Cu.

In comparison to UFG Al and Al 7075 alloys, NT Al–Ni alloys have less wear damage and reduced wear rates due to their better deformability and work hardening capability. The NT columnar grains induce good deformability that can accommodate the large microscale plasticity during scratch via column bending, grain rotation and grain coarsening as evidenced from TEM and ASTAR analysis. Furthermore, these NT columnar grains rapidly evolve into gradient nanograins during scratch, resulting in both high hardness and good structure stability at the scratch surfaces (Fig 14 (c)).

4.4 Good wear resistance of NT Al alloys

Fig. 13(c) compares the relative wear resistances (defined as the ratio between alloy and pure Al, R_W/R_W^{Al}) for NT Al-Ni alloys with other Al alloys [38,68], steels [61,65,69–71], and pure Ni [69]. The relative wear resistance of NT Al-Ni alloys is comparable to the C70 W2 tool steels [61], and much greater than nanocrystalline/amorphous Al-Ni-Sm and Al-Ni-Yi alloys that have similar hardness [38,68]. Zum Gahr and Mewes *et al.* [70,72] tested over 27 metallic materials and suggested that the wear resistance is correlated better with material work hardening capability than the material hardness. Similarly, Shi *et al.* [5] showed through MD simulations that a greater work hardening capability can induce higher wear resistance in nanocrystalline Al. As shown in Fig. 14 (a), prior studies [73,74] have shown that grain coarsening often occurs near the wear surface of nanocrystalline or UFG metals (Fig. 14(d)), resulting in work softening and degraded wear resistance of the tested material. It should be noticed that microstructure evolution mechanisms as depicted in Fig. 14 are suitable for low-speed nano scratch tests.

The outstanding wear resistance of NT Al-Ni alloys arises from the following factors. First, NT Al–Ni alloys have a much higher hardness than the UFG Al and Al 7075 alloy. Second, NT Al–Ni alloys have excellent work hardening capability under nanoscratch and thus suppress cutting chips. Third, during nanoscratch testing, high strength NT Al–Ni alloys deform plastically through column bending and grain rotation facilitated by ITB migration. Moreover, grain rotation leads to the formation of equiaxed nanograins in direct contact with the scratch tips. These nanograins can “roll” via GB sliding and thus reduce the friction between the tip and specimen. Finally, the wear-induced gradient nanograins may accommodate large plastic strain and inhibit the delamination and roughing of the wear surface, as suggested by Chen *et al.* [64].

In essence, the superior wear resistance of NT Al-Ni arises from the columnar ITBs that compose its microstructure. Apart from the high hardness and excellent work hardening capability, a high density of ITBs and SFs bring forward a special microstructure evolution pathway for Al-Ni alloys. The grain refinement in scratched NT Al-Ni alloys is facilitated by ITBs and SFs. In conventional Al alloys, deformation induced grain refinement is achieved via the gradual accumulation of dislocations, known as the continuous dynamic recrystallization (cDRX) [41]. Our scratch analyses on Al 7075 (Fig. 7 and Fig. 8) prove that there was no grain refinement. In comparison, grain refinement in NT Al-Ni alloys was caused by discontinuous dynamic recrystallization (dDRX), which refers to DRX via heterogeneous nucleation of new grains from regions full of accumulated dislocations [75]. Due to its high stacking fault energy, dislocation annihilation via cross slip and climb in Al readily occur, and the accumulation of intragranular dislocations in Al is generally insufficient to activate dDRX. However, high-density ITBs and SFs in NT Al-Ni alloys may activate the dDRX mechanism as abundant partial dislocations can nucleate from ITBs and SFs [76]. In addition, the interaction between ITBs and dislocations can further increase the dislocation density. Wei *et al* [77] showed that SFs can facilitate dDRX in UFG Al during sliding by hindering the climb and cross-slip of dislocations. Moreover, these ITBs/SFs are potential nucleation sites for new grains. The evidence from this study and literature supports our conclusion that columnar grains in NT Al-Ni alloy can rapidly evolve into gradient nanograins during scratch, contributing to their superior wear resistance.

5. Conclusions

Nanoscratch tests combined with extensive microstructural analyses have been performed to compare the tribological behaviors of UFG Al, Al 7075 and NT Al-Ni alloys. The NT Al–Ni alloys have much smaller COFs, ~ 0.39, than Al 7075, ~ 0.7. Delamination took place in UFG Al. Cutting chips formed in Al7075. In comparison, delamination, cutting chips and wear debris were absent in NT Al-Ni alloys. The wear rates of NT Al-Ni alloys are less than 10% of the UFG Al at the same applied load. Moreover, the wear resistances of NT Al-Ni alloys are five times higher than that of Al 7075 alloys. Cutting and ploughing are prevalent wear mechanisms in UFG Al and Al 7075, while micro shearing and ploughing are main wear mechanisms in NT Al-Ni alloys. Nanoscratch can lead to the accumulation of dislocation walls and gradual grain orientation change in Al 7075 without significant grain refinement. NT columnar grains can evolve into equiaxed nanograins with gradient grain size via grain rotation and ITB migration during the nanoscratch, and retain the high hardness, good work hardening ability, and good deformability under scratch. This study advances the fundamental understanding on wear mechanisms in NT metallic materials and may facilitate the design of lightweight and wear-resistant Al alloys for various applications

Acknowledgement

We acknowledge the support from the Department of energy – Basic energy Science (DOE Award number (DOE Award number: DE–SC0016337). Accesses to the Microscopy Facilities at Purdue University and DOE-Center for Integrated Nanotechnologies (managed by Los Alamos National laboratory) are also acknowledged.

References

[1] K. Holmberg, A. Erdemir, Influence of tribology on global energy consumption, costs and emissions, Friction. 5 (2017) 263–284.

[2] C. Vargel, Corrosion of aluminium, Elsevier, 2020.

[3] J.R. Davis, Aluminum and aluminum alloys, ASM international, 1993.

[4] E.A. Starke Jr, J.T. Staley, Application of modern aluminum alloys to aircraft, Prog. Aerosp. Sci. 32 (1996) 131–172.

[5] Y. Shi, I. Szlufarska, Wear-induced microstructural evolution of nanocrystalline aluminum and the role of zirconium dopants, Acta Mater. 200 (2020) 432–441. https://doi.org/10.1016/j.actamat.2020.09.005.

[6] Y. Wang, Y. Zhu, D. Zhao, D. Bian, Nanoscratch of aluminum in dry, water and aqueous H 2 O 2 conditions, Appl. Surf. Sci. 464 (2019) 229–235. https://doi.org/10.1016/j.apsusc.2018.09.075.

[7] J. Zhang, A.T. Alpas, Transition between mild and severe wear in aluminium alloys, Acta Mater. 45 (1997) 513–528. https://doi.org/10.1016/S1359-6454(96)00191-7.

[8] V. Bhattacharya, K. Chattopadhyay, Microstructure and wear behaviour of aluminium alloys containing embedded nanoscaled lead dispersoids, Acta Mater. 52 (2004) 2293–2304. https://doi.org/10.1016/j.actamat.2004.01.020.

[9] J. Goddard, H. Wilman, A theory of friction and wear during the abrasion of metals, Wear. 5 (1962) 114–135.

[10] M. Varenberg, Towards a unified classification of wear, Friction. 1 (2013) 333–340. https://doi.org/10.1007/s40544-013-0027-x.

[11] Y.X. Ye, C.Z. Liu, H. Wang, T.G. Nieh, Friction and wear behavior of a single-phase equiatomic TiZrHfNb high-entropy alloy studied using a nanoscratch technique, Acta Mater. 147 (2018) 78–89. https://doi.org/10.1016/j.actamat.2018.01.014.

[12] N. Xu, W. Han, Y. Wang, J. Li, Z. Shan, Nanoscratching of copper surface by CeO2, Acta Mater. 124 (2017) 343–350. https://doi.org/10.1016/j.actamat.2016.11.008.

[13] B.D. Beake, V.M. Vishnyakov, A.J. Harris, Nano-scratch testing of (Ti,Fe)Nx thin films on silicon, Surf. Coatings Technol. 309 (2017) 671–679. https://doi.org/10.1016/j.surfcoat.2016.11.024.

[14] B.D. Beake, A.J. Harris, T.W. Liskiewicz, Review of recent progress in nanoscratch testing, Tribol. - Mater. Surfaces Interfaces. 7 (2013) 87–96. https://doi.org/10.1179/1751584X13Y.0000000037.

[15] A.M. Hodge, T.G. Nieh, Evaluating abrasive wear of amorphous alloys using nanoscratch technique, Intermetallics. 12 (2004) 741–748. https://doi.org/10.1016/j.intermet.2004.02.014.

[16] G. Subhash, W. Zhang, Investigation of the overall friction coefficient in single-pass scratch test, Wear. 252 (2002) 123–134.

[17] S.M. Noh, J.W. Lee, J.H. Nam, J.M. Park, H.W. Jung, Analysis of scratch characteristics of automotive clearcoats containing silane modified blocked isocyanates via carwash and nano-scratch tests, Prog. Org. Coatings. 74 (2012) 192–203.

[18] Q. Jia, W. He, D. Hua, Q. Zhou, Y. Du, Y. Ren, Z. Lu, H. Wang, F. Zhou, J. Wang, Effects of structure relaxation and surface oxidation on nanoscopic wear behaviors of metallic glass, Acta Mater. 232 (2022) 117934. https://doi.org/10.1016/j.actamat.2022.117934.

[19] D. Luo, Q. Zhou, W. Ye, Y. Ren, C. Greiner, Y. He, H. Wang, Design and Characterization of Self-Lubricating Refractory High Entropy Alloy-Based Multilayered Films, ACS Appl. Mater. Interfaces. 13 (2021) 55712–55725. https://doi.org/10.1021/acsami.1c16949.

[20] W. Wang, K. Wang, Z. Zhang, J. Chen, T. Mou, F.M. Michel, H. Xin, W. Cai, Ultrahigh tribocorrosion resistance of metals enabled by nano-layering, Acta Mater. 206 (2021) 116609. https://doi.org/10.1016/j.actamat.2020.116609.

[21] Y. Wang, Y. Zhu, D. Zhao, D. Bian, Nanoscratch of aluminum in dry, water and aqueous H 2 O 2 conditions, Appl. Surf. Sci. 464 (2019) 229–235. https://doi.org/10.1016/j.apsusc.2018.09.075.

[22] H.H. Kim, S.H. Cho, C.G. Kang, Evaluation of microstructure and mechanical properties by using nano/micro-indentation and nanoscratch during aging treatment of rheo-forged Al 6061 alloy, Mater. Sci. Eng. A. 485 (2008) 272–281. https://doi.org/10.1016/j.msea.2007.07.085.

[23] L. Huang, T.D. Topping, H. Yang, E.J. Lavernia, J.M. Schoenung, Nanoscratch-induced deformation behaviour in B 4C particle reinforced ultrafine grained Al alloy composites: A novel diagnostic approach, Philos. Mag. 94 (2014) 1754–1763. https://doi.org/10.1080/14786435.2014.895442.

[24] N. Kang, P. Coddet, H. Liao, T. Baur, C. Coddet, Wear behavior and microstructure of hypereutectic Al-Si alloys prepared by selective laser melting, Appl. Surf. Sci. 378 (2016) 142–149.

[25] J.S.S. Babu, A. Srinivasan, C.G. Kang, Tribological and nano-scratch properties of aluminum (A356) based hybrid composites reinforced with MWCNTs/alumina fiber, Met. Mater. Int. (2020)

1–15.

[26] J. Qu, H. Xu, Z. Feng, D.A. Frederick, L. An, H. Heinrich, Improving the tribological characteristics of aluminum 6061 alloy by surface compositing with sub-micro-size ceramic particles via friction stir processing, Wear. 271 (2011) 1940–1945.

[27] X. Zhang, A. Misra, H. Wang, T.D. Shen, M. Nastasi, T.E. Mitchell, J.P. Hirth, R.G. Hoagland, J.D. Embury, Enhanced hardening in Cu/330 stainless steel multilayers by nanoscale twinning, Acta Mater. 52 (2004) 995–1002. https://doi.org/10.1016/j.actamat.2003.10.033.

[28] O. Anderoglu, A. Misra, H. Wang, X. Zhang, Thermal stability of sputtered Cu films with nanoscale growth twins, J. Appl. Phys. 103 (2008) 94322. https://doi.org/10.1063/1.2913322.

[29] Y.F. Zhang, R. Su, T.J. Niu, N.A. Richter, S. Xue, Q. Li, J. Ding, B. Yang, H. Wang, X. Zhang, Thermal stability and deformability of annealed nanotwinned Al/Ti multilayers, Scr. Mater. 186 (2020) 219–224.

[30] T. Niu, J. Li, Y. Zhang, J. Cho, J. Ding, R. Su, S. Xue, C. Fan, Z. Shang, D. Chen, In-situ Studies on the Mechanical Properties of He Ion Irradiated Nanotwinned Ag, J. Nucl. Mater. (2020) 152392.

[31] J. Yan, A. Lindo, R. Schwaiger, A.M. Hodge, Sliding wear behavior of fully nanotwinned Cu alloys, Friction. 7 (2019) 260–267. https://doi.org/10.1007/s40544-018-0220-z.

[32] I.J. Beyerlein, X. Zhang, A. Misra, Growth twins and deformation twins in metals, Annu. Rev. Mater. Res. 44 (2014) 329–363.

[33] Y.F. Zhang, R. Su, D.Y. Xie, T.J. Niu, S. Xue, Q. Li, Z. Shang, J. Ding, N.A. Richter, J. Wang, H. Wang, X. Zhang, Design of super-strong and thermally stable nanotwinned Al alloys via solute synergy, Nanoscale. 12 (2020). https://doi.org/10.1039/d0nr05707j.

[34] Y.F. Zhang, Q. Li, S.C. Xue, J. Ding, D.Y. Xie, J. Li, T. Niu, H. Wang, H. Wang, J. Wang, X. Zhang, Ultra-strong nanotwinned Al–Ni solid solution alloys with significant plasticity, Nanoscale. 10 (2018) 22025–22034. https://doi.org/10.1039/c8nr05139a.

[35] E.F. Rauch, J. Portillo, S. Nicolopoulos, D. Bultreys, S. Rouvimov, P. Moeck, Automated nanocrystal orientation and phase mapping in the transmission electron microscope on the basis

of precession electron diffraction, Zeitschrift Für Krist. Int. J. Struct. Phys. Chem. Asp. Cryst. Mater. 225 (2010) 103–109.

[36] W.C. Oliver, G.M. Pharr, An improved technique for determining hardness and elastic modulus using load and displacement sensing indentation experiments, J. Mater. Res. 7 (1992) 1564–1583.

[37] J.F. Archard, Contact and rubbing of flat surfaces, J. Appl. Phys. 24 (1953) 981–988. https://doi.org/10.1063/1.1721448.

[38] A.L. Greer, K.L. Rutherford, I.M. Hutchings, Wear resistance of amorphous alloys and related materials, Int. Mater. Rev. 47 (2002) 87–112.

[39] I. Alabd Alhafez, C.J. Ruestes, H.M. Urbassek, Size of the Plastic Zone Produced by Nanoscratching, Tribol. Lett. 66 (2018) 1–12. https://doi.org/10.1007/s11249-017-0967-9.

[40] A. Li, I. Szlufarska, How grain size controls friction and wear in nanocrystalline metals, Phys. Rev. B - Condens. Matter Mater. Phys. 92 (2015). https://doi.org/10.1103/PhysRevB.92.075418.

[41] T. Sakai, A. Belyakov, R. Kaibyshev, H. Miura, J.J. Jonas, Dynamic and post-dynamic recrystallization under hot, cold and severe plastic deformation conditions, Prog. Mater. Sci. 60 (2014) 130–207.

[42] J.C.M. Li, Petch relation and grain boundary sources, Trans. Met. Soc. AIME. 227 (1963) 239.

[43] A.K. Talachi, M. Eizadjou, H.D. Manesh, K. Janghorban, Wear characteristics of severely deformed aluminum sheets by accumulative roll bonding (ARB) process, Mater. Charact. 62 (2011) 12–21.

[44] F.J. Humphreys, M. Hatherly, Recrystallization and related annealing phenomena, Elsevier, 2012.

[45] J. Wang, O. Anderoglu, J.P. Hirth, A. Misra, X. Zhang, Dislocation structures of σ3 {112} twin boundaries in face centered cubic metals, Appl. Phys. Lett. 95 (2009) 93–96. https://doi.org/10.1063/1.3176979.

[46] Z. Wang, J. Li, Q.H. Fang, B. Liu, L. Zhang, Investigation into nanoscratching mechanical response of AlCrCuFeNi high-entropy alloys using atomic simulations, Appl. Surf. Sci. 416 (2017) 470–481. https://doi.org/10.1016/j.apsusc.2017.04.009.

[47] X. Ma, B. Gwalani, J. Tao, M. Efe, M. Olszta, M. Song, S. Yadav, A. Yu, T.J. Nizolek, J.S.

Carpenter, Shear strain gradient in Cu/Nb nanolaminates: strain accommodation and chemical mixing, Acta Mater. (2022) 117986.

[48] H.G. Howell, J. Mazur, Amontons' law and fibre friction, J. Text. Inst. Trans. 44 (1953) T59–T69. https://doi.org/10.1080/19447025308659728.

[49] F.P. Bowden, D. Tabor, The friction and lubrification of solids, Clarendon press, 1954.

[50] S. Lafaye, M. Troyon, On the friction behaviour in nanoscratch testing, Wear. 261 (2006) 905–913. https://doi.org/10.1016/j.wear.2006.01.036.

[51] S.R. Bakshi, D. Lahiri, R.R. Patel, A. Agarwal, Nanoscratch behavior of carbon nanotube reinforced aluminum coatings, Thin Solid Films. 518 (2010) 1703–1711. https://doi.org/10.1016/j.tsf.2009.11.079.

[52] S. Lafaye, C. Gauthier, R. Schirrer, The ploughing friction: Analytical model with elastic recovery for a conical tip with a blunted spherical extremity, Tribol. Lett. 21 (2006) 95–99. https://doi.org/10.1007/s11249-006-9018-7.

[53] I. Alabd Alhafez, A. Brodyanski, M. Kopnarski, H.M. Urbassek, Influence of Tip Geometry on Nanoscratching, Tribol. Lett. 65 (2017). https://doi.org/10.1007/s11249-016-0804-6.

[54] N. Kang, P. Coddet, H. Liao, T. Baur, C. Coddet, Wear behavior and microstructure of hypereutectic Al-Si alloys prepared by selective laser melting, Appl. Surf. Sci. 378 (2016) 142–149. https://doi.org/10.1016/j.apsusc.2016.03.221.

[55] B. Venkataraman, G. Sundararajan, Correlation between the characteristics of the mechanically mixed layer and wear behaviour of aluminium, Al-7075 alloy and Al-MMCs, Wear. 245 (2000) 22–38. https://doi.org/10.1016/S0043-1648(00)00463-4.

[56] M. Tocci, A. Pola, L. Girelli, F. Lollio, L. Montesano, M. Gelfi, Wear and cavitation erosion resistance of an ALMgSC alloy produced by DMLS, Metals (Basel). 9 (2019). https://doi.org/10.3390/met9030308.

[57] J. Qu, H. Xu, Z. Feng, D.A. Frederick, L. An, H. Heinrich, Improving the tribological characteristics of aluminum 6061 alloy by surface compositing with sub-micro-size ceramic particles via friction stir processing, Wear. 271 (2011) 1940–1945.

https://doi.org/10.1016/j.wear.2010.11.046.

[58] S.R. Bakshi, D. Lahiri, R.R. Patel, A. Agarwal, Nanoscratch behavior of carbon nanotube reinforced aluminum coatings, Thin Solid Films. 518 (2010) 1703–1711.

[59] J.S.S. Babu, A. Srinivasan, C.G. Kang, Tribological and Nano-Scratch Properties of Aluminum (A356) Based Hybrid Composites Reinforced with MWCNTs/Alumina Fiber, Met. Mater. Int. (2020). https://doi.org/10.1007/s12540-020-00787-6.

[60] K. Hokkirigawa, K. Kato, An experimental and theoretical investigation of ploughing, cutting and wedge formation during abrasive wear, Tribol. Int. 21 (1988) 51–57. https://doi.org/10.1016/0301-679X(88)90128-4.

[61] K.H. Zum Gahr, Modelling of two-body abrasive wear, Wear. 124 (1988) 87–103.

[62] M. Wen, C. Wen, P.D. Hodgson, Y.C. Li, Tribological behaviour of pure Ti with a nanocrystalline surface layer under different loads, Tribol. Lett. 45 (2012) 59–66. https://doi.org/10.1007/s11249-011-9862-y.

[63] Y.S. Zhang, Z. Han, K. Wang, K. Lu, Friction and wear behaviors of nanocrystalline surface layer of pure copper, Wear. 260 (2006) 942–948. https://doi.org/10.1016/j.wear.2005.06.010.

[64] X. Chen, Z. Han, X. Li, K. Lu, Lowering coefficient of friction in cu alloys with stable gradient nanostructures, Sci. Adv. 2 (2016) 1–8. https://doi.org/10.1126/sciadv.1601942.

[65] K. Kato, Micro-mechanisms of wear - wear modes, Wear. 153 (1992) 277–295. https://doi.org/10.1016/0043-1648(92)90274-C.

[66] D. Ghosh, G. Subhash, R. Radhakrishnan, T.S. Sudarshan, Scratch-induced microplasticity and microcracking in zirconium diboride-silicon carbide composite, Acta Mater. 56 (2008) 3011–3022. https://doi.org/10.1016/j.actamat.2008.02.038.

[67] K.-H. Zum Gahr, Formation of wear debris by the abrasion of ductile metals, Wear. 74 (1981) 353–373.

[68] T. Gloriant, A.L. Greer, Al-based nanocrystalline composites by rapid solidification of Al-Ni-Sm alloys, Nanostructured Mater. 10 (1998) 389–396.

[69] K. Hokkirigawa, K. Kato, Z.Z. Li, The effect of hardness on the transition of the abrasive wear

mechanism of steels, Wear. 123 (1988) 241–251. https://doi.org/10.1016/0043-1648(88)90102-0.

[70] K.H. Zum Gahr, D. Mewes, Severity of material removal in abrasive wear of ductile metals, Wear Mater. 1983. (1983) 130–139.

[71] L. Xu, N.F. Kennon, A study of the abrasive wear of carbon steels, Wear. 148 (1991) 101–112.

[72] D. Mewes, K.H. Zum Gahr, Abrasiwerschleiss duktiler Metalle, Werkstoffpriifung, 1984, DVM, Berlin. (1985) 403–415.

[73] T.J. Rupert, C.A. Schuh, Sliding wear of nanocrystalline Ni–W: structural evolution and the apparent breakdown of Archard scaling, Acta Mater. 58 (2010) 4137–4148.

[74] Y.S. Kim, T.O. Lee, D.H. Shin, Microstructural evolution and mechanical properties of ultrafine grained commercially pure 1100 aluminum alloy processed by accumulative roll-bonding (ARB), in: Mater. Sci. Forum, Trans Tech Publ, 2004: pp. 625–628.

[75] K. Huang, R.E. Logé, A review of dynamic recrystallization phenomena in metallic materials, Mater. Des. 111 (2016) 548–574.

[76] D. Bufford, Y. Liu, J. Wang, H. Wang, X. Zhang, In situ nanoindentation study on plasticity and work hardening in aluminium with incoherent twin boundaries, Nat. Commun. 5 (2014) 4864. https://doi.org/10.1038/ncomms5864.

[77] S. Wei, H. Zhang, C. Tangpatjaroen, J. Tarnsangpradit, A.D. Usta, M. Eriten, J.H. Perepezko, I. Szlufarska, Wear-induced microstructural evolution of ultra-fine grained (UFGs) aluminum, Acta Mater. 209 (2021) 116787.

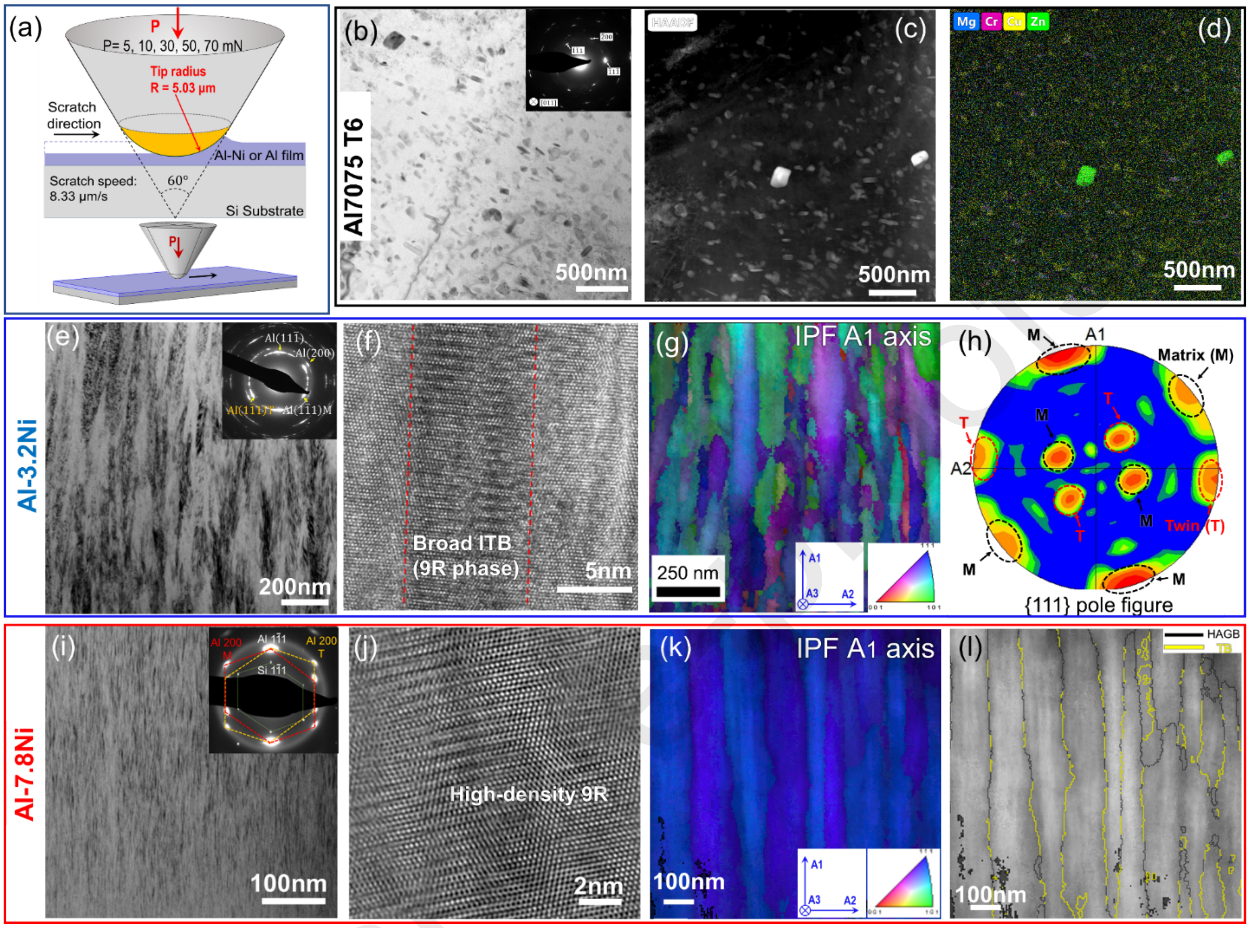

Figure 1. (a) Schematics illustrating the nanoscratch setups, including geometry of indenter, normal applied load (*P*) and scratch speed for high-load nano scratch tests. Bright-field (BF) TEM (b) and HAADF STEM (c) images showing high-density precipitates in the as-received Al 7075 sample. (d) EDS map showing the distributions of Cu, Cr, Zn, and Mg solutes. (e) BF cross-section TEM (XTEM) micrograph with inserted selected area diffraction (SAD) pattern showing polycrystal Al-3.2 Ni alloys with twins. (f) HRTEM image showing the broad ITB (9R) in Al-3.2Ni. (g) ASTAR inverse pole figure (IPF) orientation map showing columnar grains with in-plane rotations in Al-3.2Ni. (h) ASTAR pole figure showing the existence of twins in Al-3.2Ni alloy. (i) BF XTEM micrographs with SAD pattern showing nanotwinned columns in Al-7.8Ni with an average grain size of 7 nm. (j) High-resolution TEM (HRTEM) image showing 9R phases. (k) ASTAR IPF orientation map showing the {111} texture of Al-7.8Ni. (l) Image quality (IQ) map with ∑3 twin boundaries (TBs) and high-angle grain boundaries (HAGBs) in Al-7.8Ni.

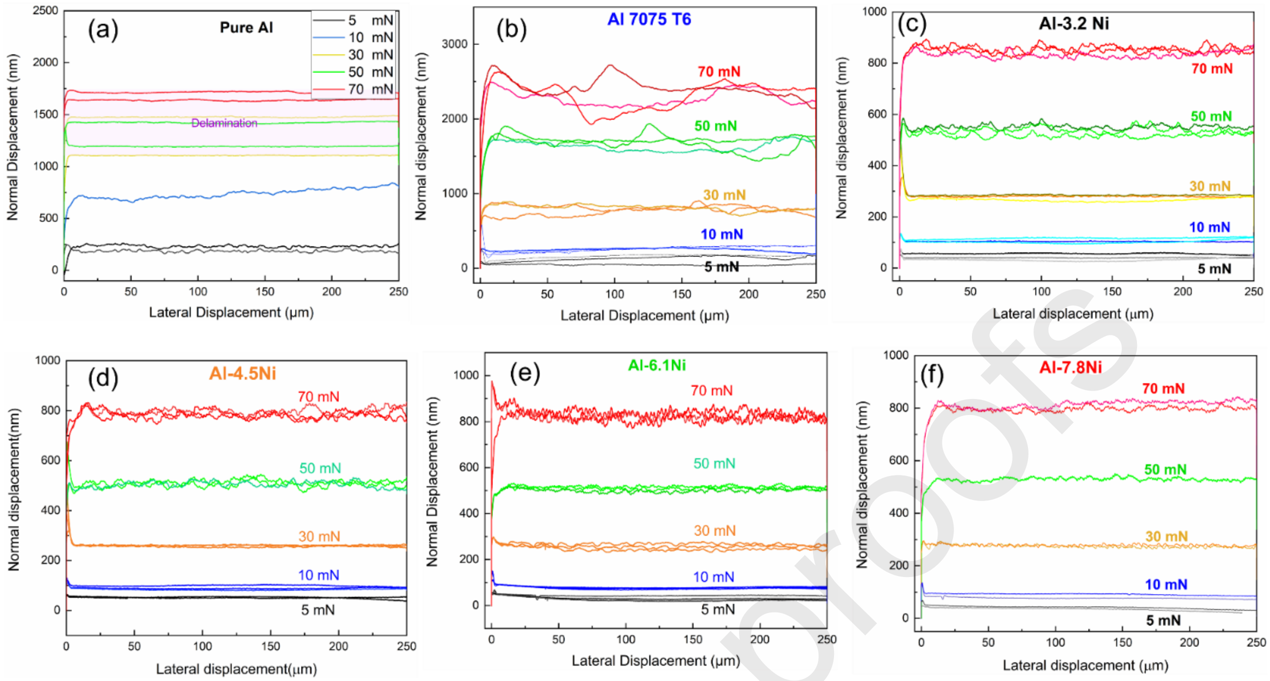

Figure 2. Plots of total normal displacements of indenters as a function of the lateral displacement for (a) UFG Al film, (b) Al 7075, and (c-f) nanotwinned Al-Ni alloys at different applied loads ranging from 5 to 70 mN.

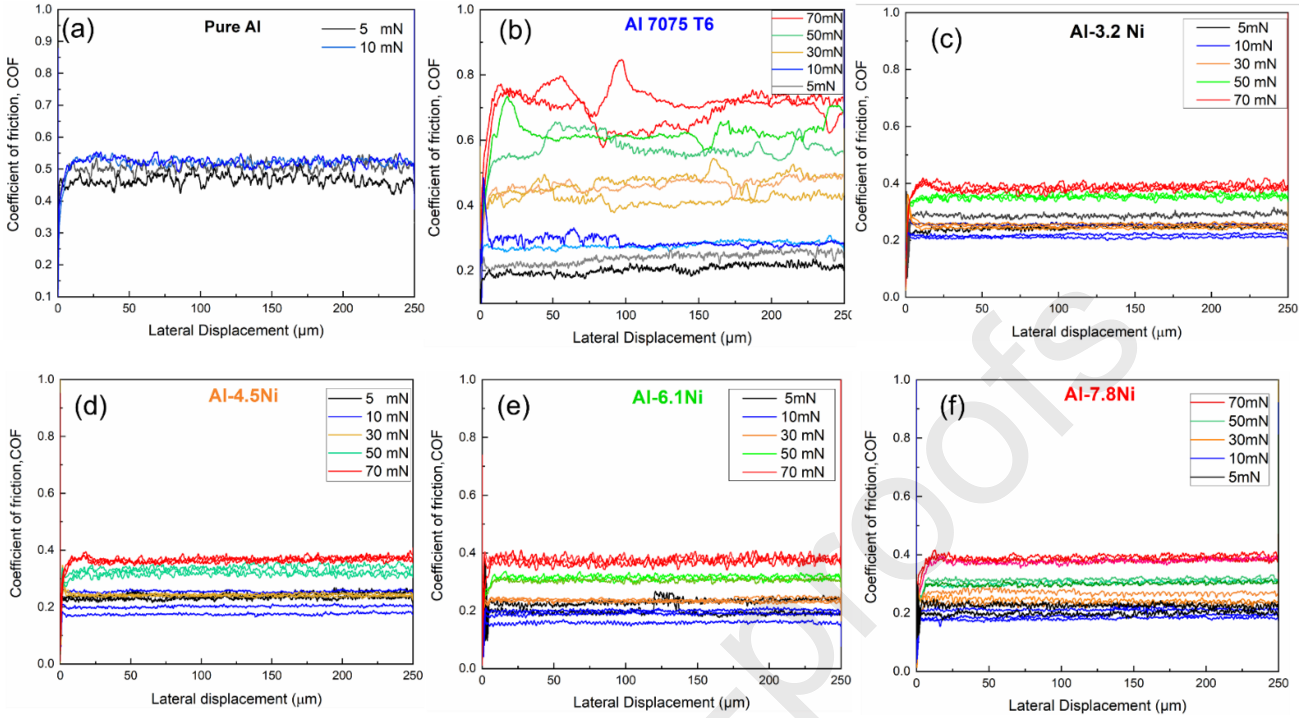

Figure 3. The coefficient of friction (COF) plotted against the lateral displacement at different normal applied loads for (a) Al, (b) Al 7075, and (c-f) NT Al-Ni alloys.

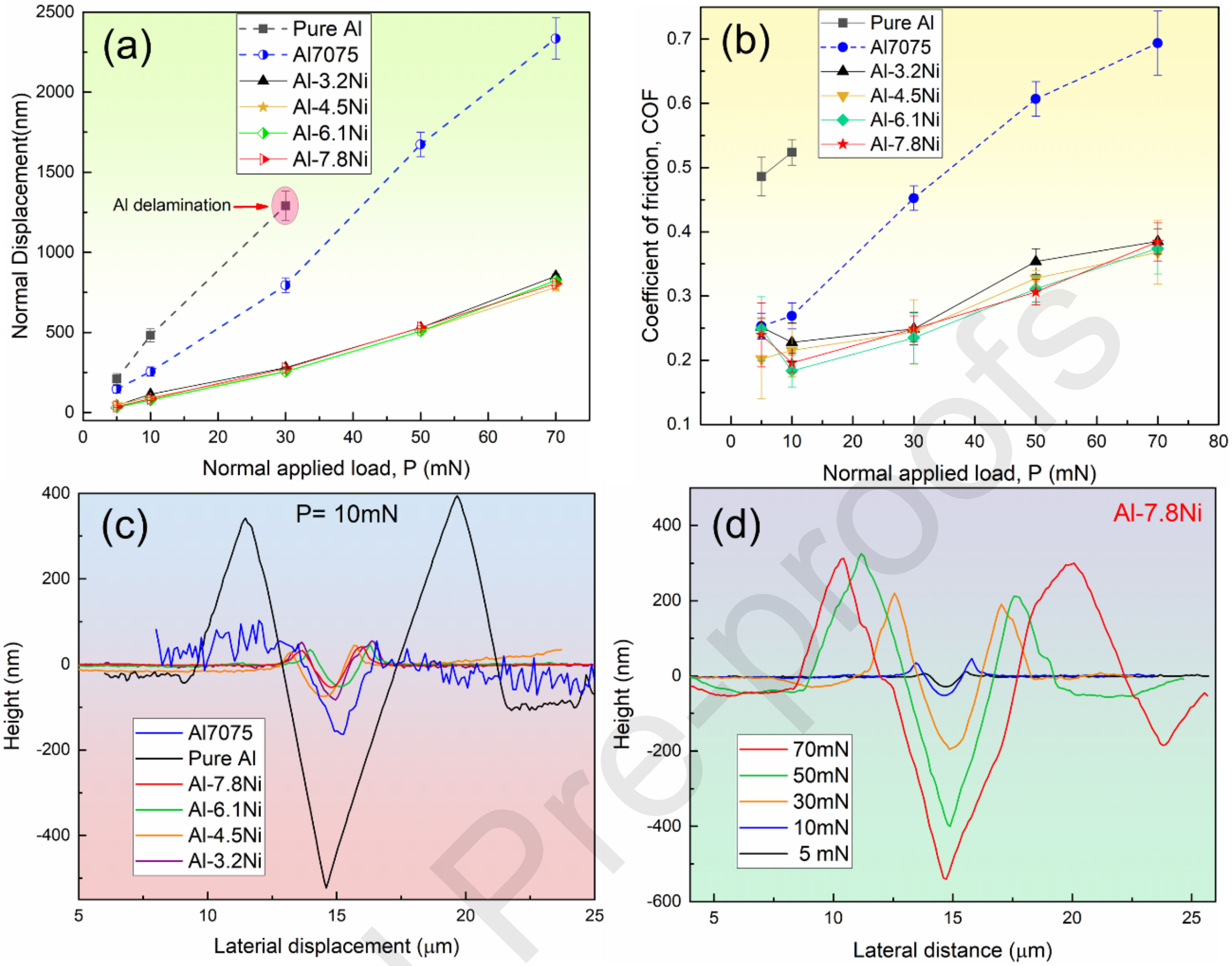

Figure 4. Results of nanoscratch tests. (a) The total normal displacement of indenter plotted as a function of normal applied load for different materials. (b) The variation of COFs with the normal applied load. (c) Cross-section depth profiles of scratch sites on Al-7.8Ni collected by SPM. (d) Cross-section depth profiles of scratch sites on different samples at the normal applied load (*P*) of 10 mN.

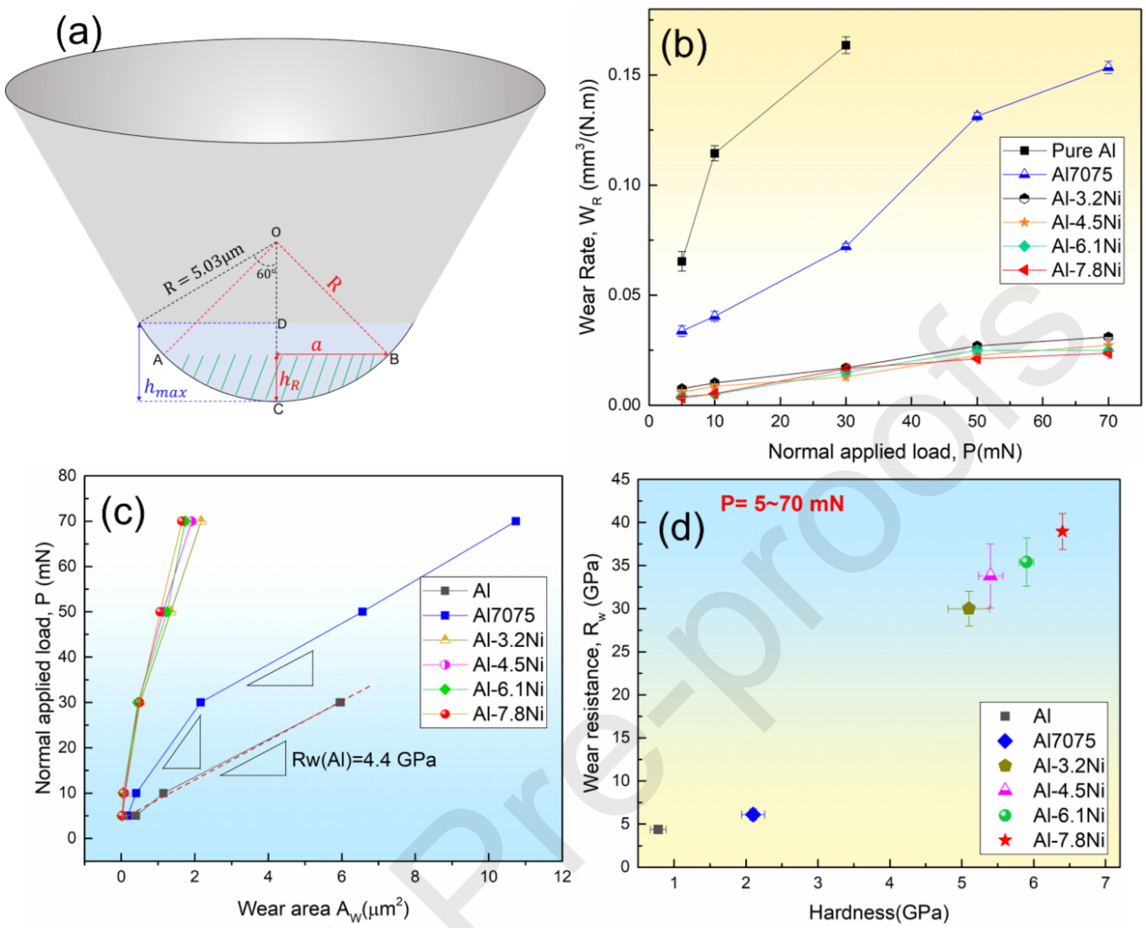

Figure 5. (a) The schematic showing the calculation of wear areas (A_w) by using the residual wear depth (h_R). (b) Calculated wear rates plotted as a function of normal applied loads for different samples. (c) Plots of applied normal load (P) against the cross-section wear area (A_w) used for the calculation of wear resistance. (d) Plots of wear resistance (R_w) against the hardness of samples.

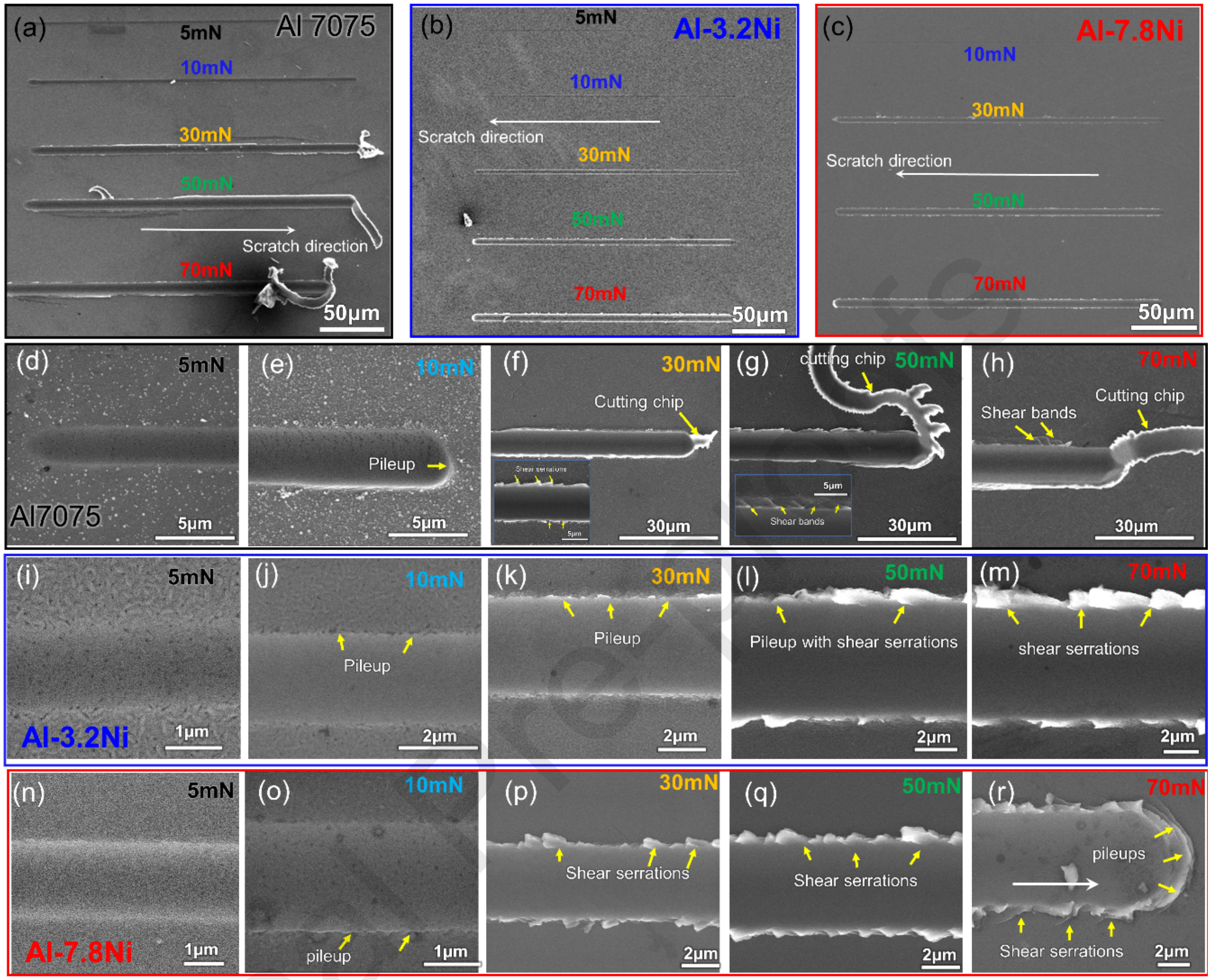

Figure 6. Scanning electron microscopy (SEM) images showing the overview of scratch sites on (a) Al7075, (b) Al-3.2Ni, and (c) Al-7.8Ni. (d-h) SEM images of scratch sites on Al 7075 sample showing material pile-ups near the end of the groove. (i-k) SEM images showing pile-ups at the edge of the scratch grooves in NT Al-3.2Ni when $P \leq 30$ mN. (l-m) Shear serrations emerged at the edge of scratch sites in NT Al-3.2Ni when $P \geq 50$ mN. Debris or cutting chips are absent. (n-r) SEM images showing the morphologies of scratch grooves on NT Al-7.8Ni. Scratch traces were smooth without shear bands when $P \leq 10$ mN. Shear serrations appeared along edges of scratch sites when $P \geqslant 30$ mN.

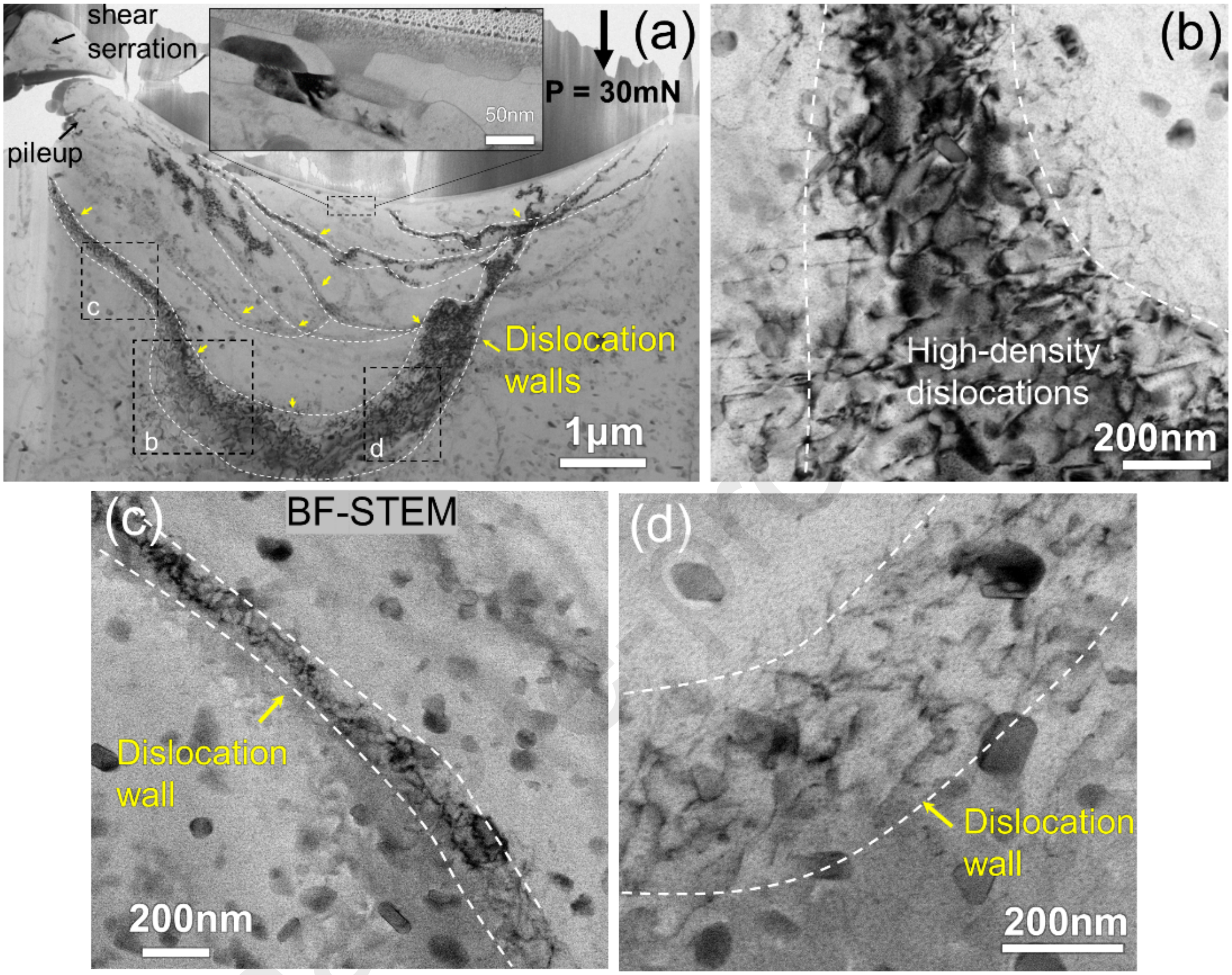

Figure 7. (a) Low-mag BF TEM images showing micron-scale dislocation bands beneath the indenter and the aggregated precipitates ($MgZn_2$) near the scratch surfaces of Al 7075 alloy. The zone axis is parallel with the scratch direction. (b) BF TEM image and BF STEM images (c-d) demonstrating the high-density dislocations within the dislocation bands.

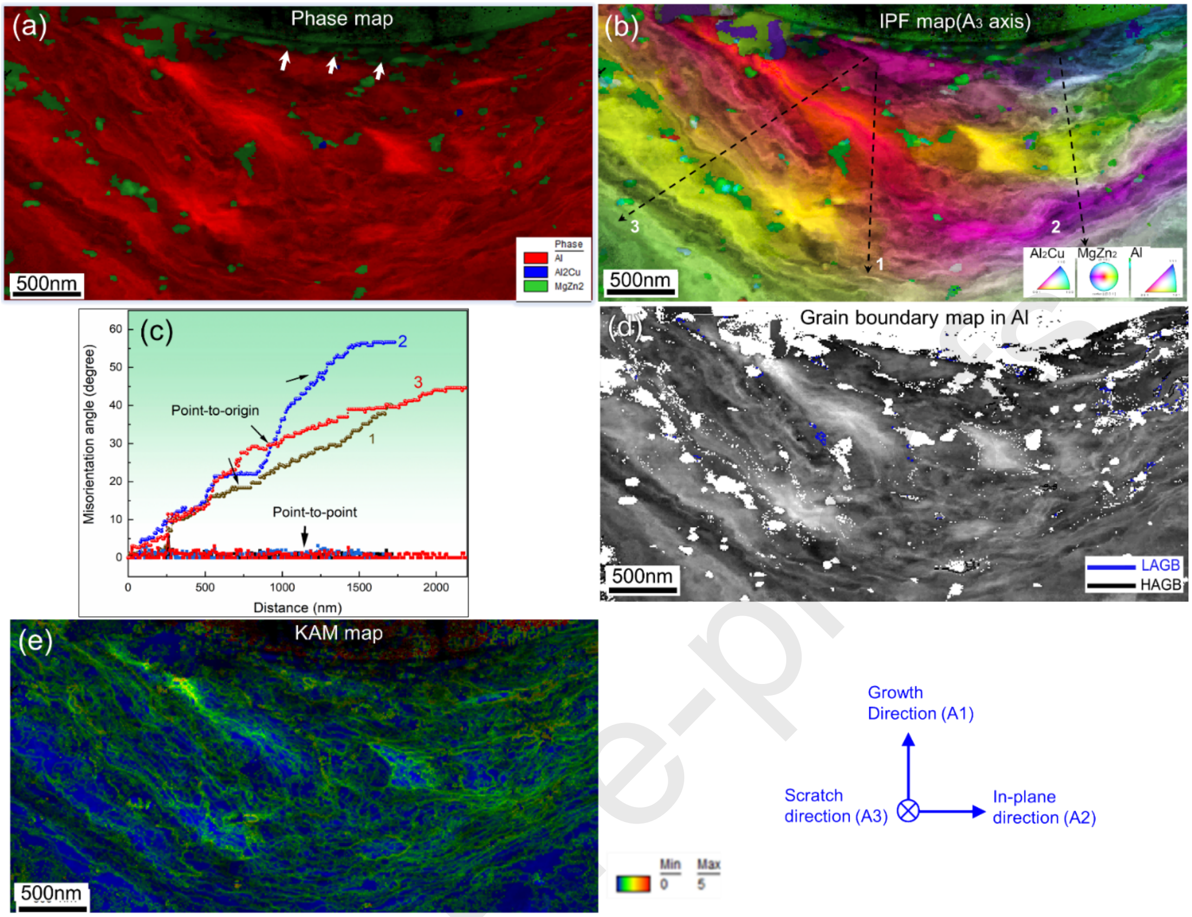

Figure 8. ASTAR crystal orientation analyses on the scratch sites of Al 7075. (a) ASTAR phase map of the scratch site showing abundant $MgZn_2$ and scattered Al_2Cu nano precipitates. (b) IPF orientation map with misorientation line-scan profiles (c) prove the gradual orientation evolution from the scratch surface to the matrix. (d) Image quality (IQ) map with grain boundaries (GBs) in Al after scratch. (e) Kernel average misorientation (KAM) map of scratch regions under the scratch surface.

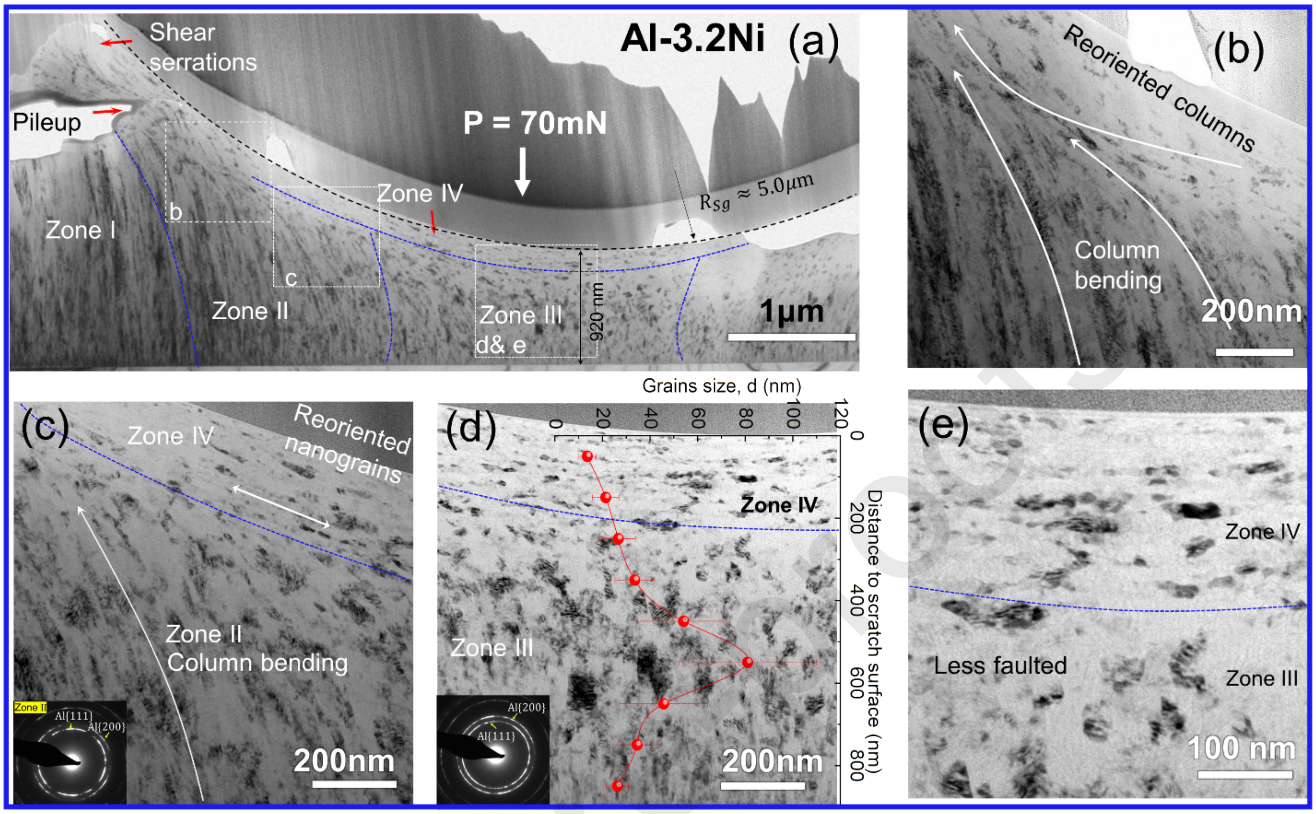

Figure 9. (a) BF XTEM image showing the microstructure along the scratch groove of Al-3.2Ni. (b) BF TEM image taken from upper left corner of the scratch site showing the column bending and the reoriented columns near the scratch surface. (c) BF TEM image showing bended columns in the transition zone III, and the reoriented nanolaminates in zone IV. (d) BF TEM image showing the gradient nanograins beneath the indenter. The superimposed plot shows the variation of grain size along normal direction. (e) Magnified BF TEM micrograph showing the less-faulted zone IV& III.

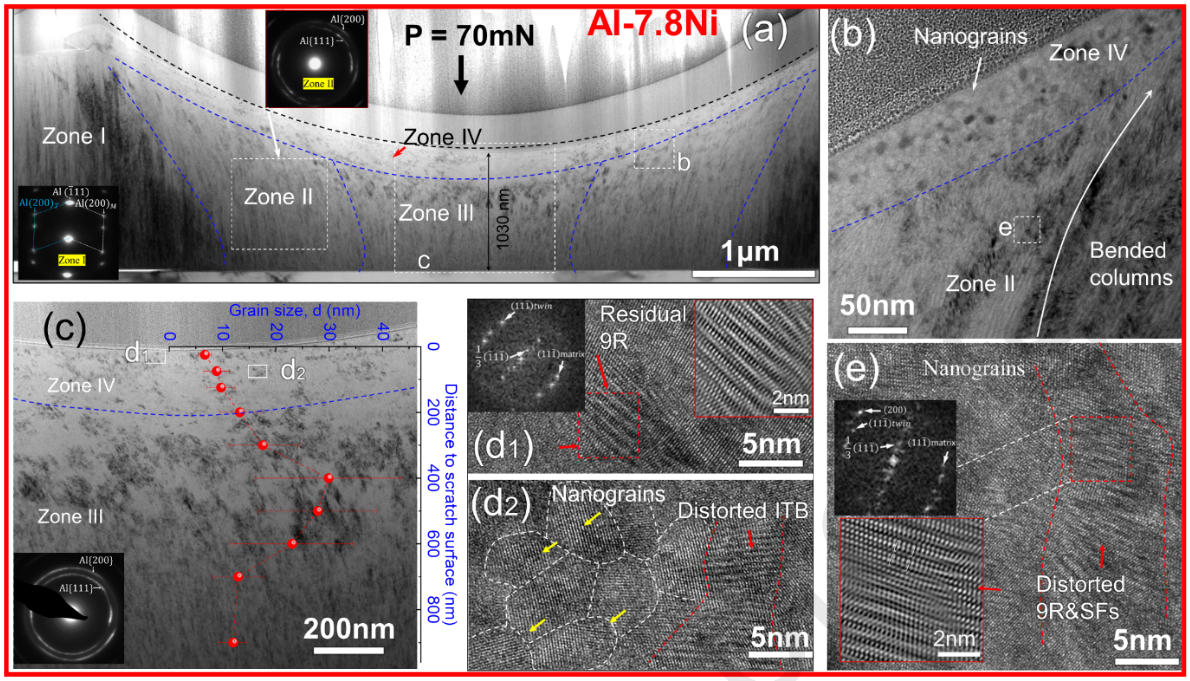

Figure 10. (a) BF XTEM image showing the scratch site of Al-7.8 Ni. (b) BF TEM image showing bended columns in the transition zone II, and nanograins in zone IV near the scratch surface. (c) Magnified BF TEM image and grain size distribution beneath the indenter. (d_1-d_2) HRTEM images showing nanograins and distorted ITB (broad 9R phase) in zone IV. (e) HRTEM images with inserted fast Fourier transform (FFT) patterns showing the detwinning of 9R phase and its evolution into nanograins in zone II.

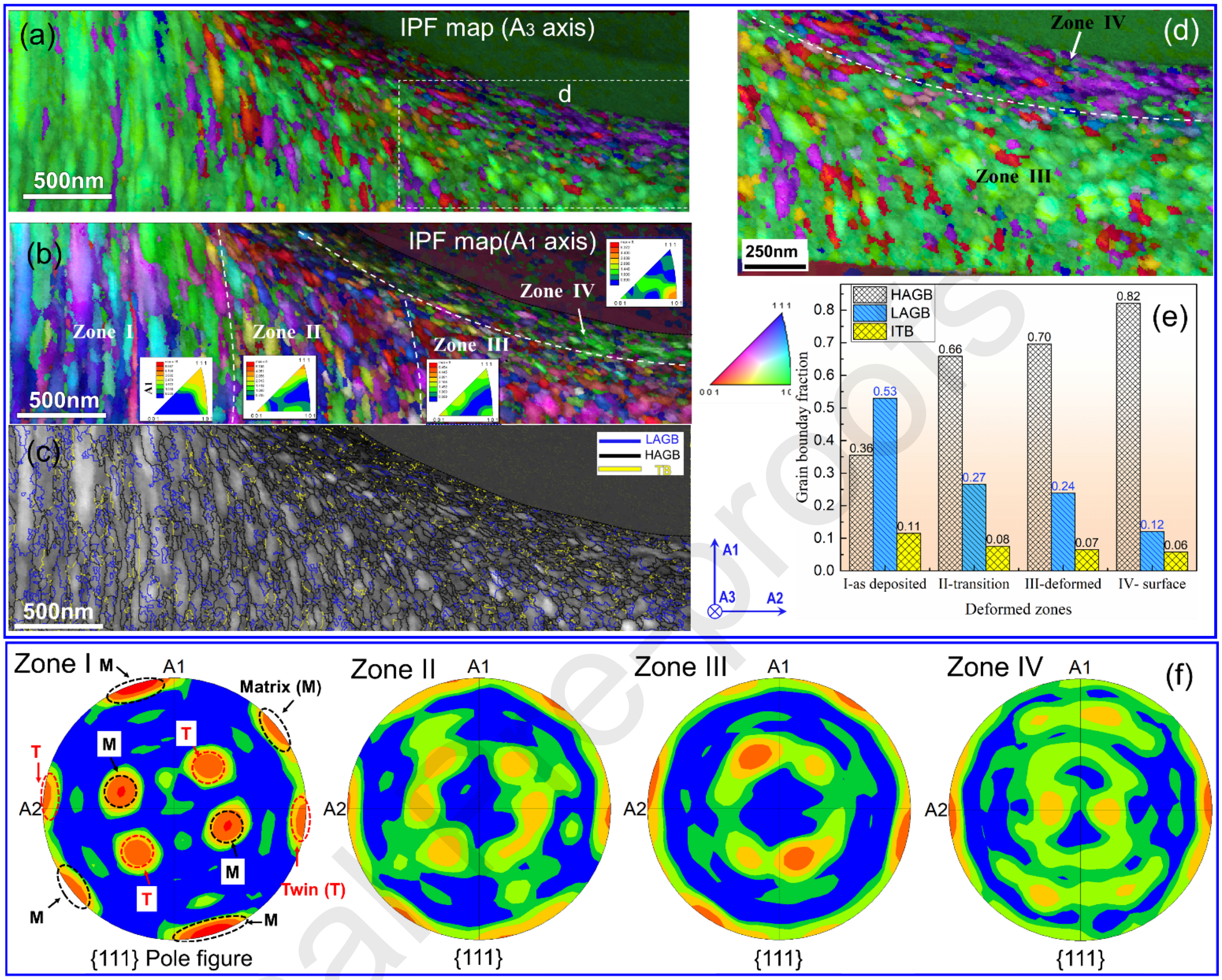

Figure 11. ASTAR analyses of Al-3.2Ni under the applied load of 70 mN. (a-b) IPF orientation maps of the scratch site of Al-3.2Ni collected from A_3 (scratch direction) and A_1 axis (growth direction), respectively. (c) IQ image with different types of GBs. (d) Magnified IPF orientation map of the region beneath the indenter. (e) Statistics showing the fraction of HAGBs and LAGBs and ITBs at different zones (I-IV) near the scratch site. (f) {111}pole figure maps from different zones on the scratch sites of Al-3.2Ni.

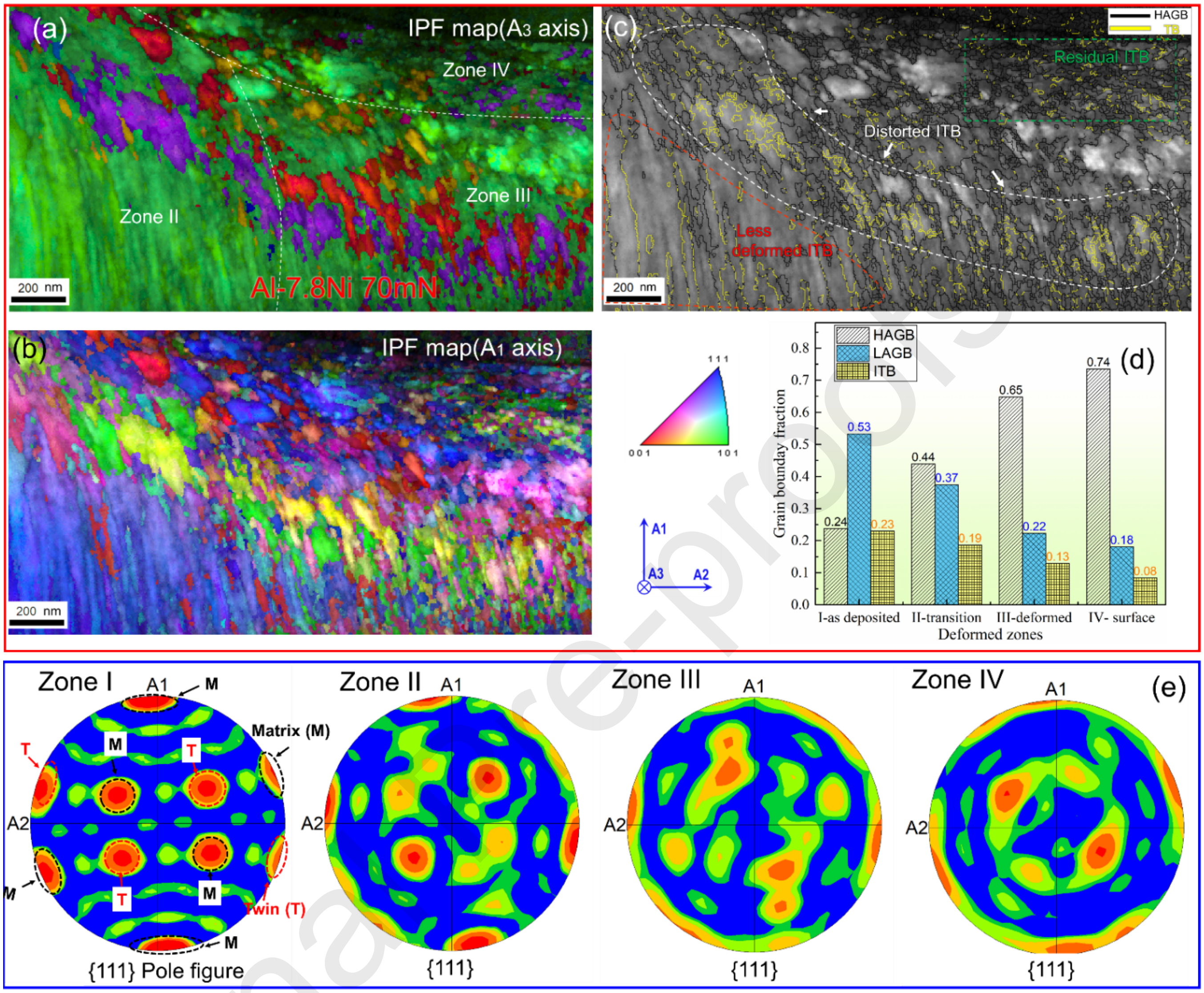

Figure 12. (a-b) ASTAR IPF orientation map of scratch site of Al-7.8Ni. (c) IQ map with HAGBs and TBs on the scratch site of Al-7.8 Ni. ITBs with different morphologies are highlighted by using red, white, and green dash boxes. (d) Statistics showing the fraction of HAGBs and LAGBs and ITBs at different zones (I-IV) on the scratch site of Al -7.8Ni. (e) {111}pole figure maps from different zones on the scratch sites of Al-7.8Ni.

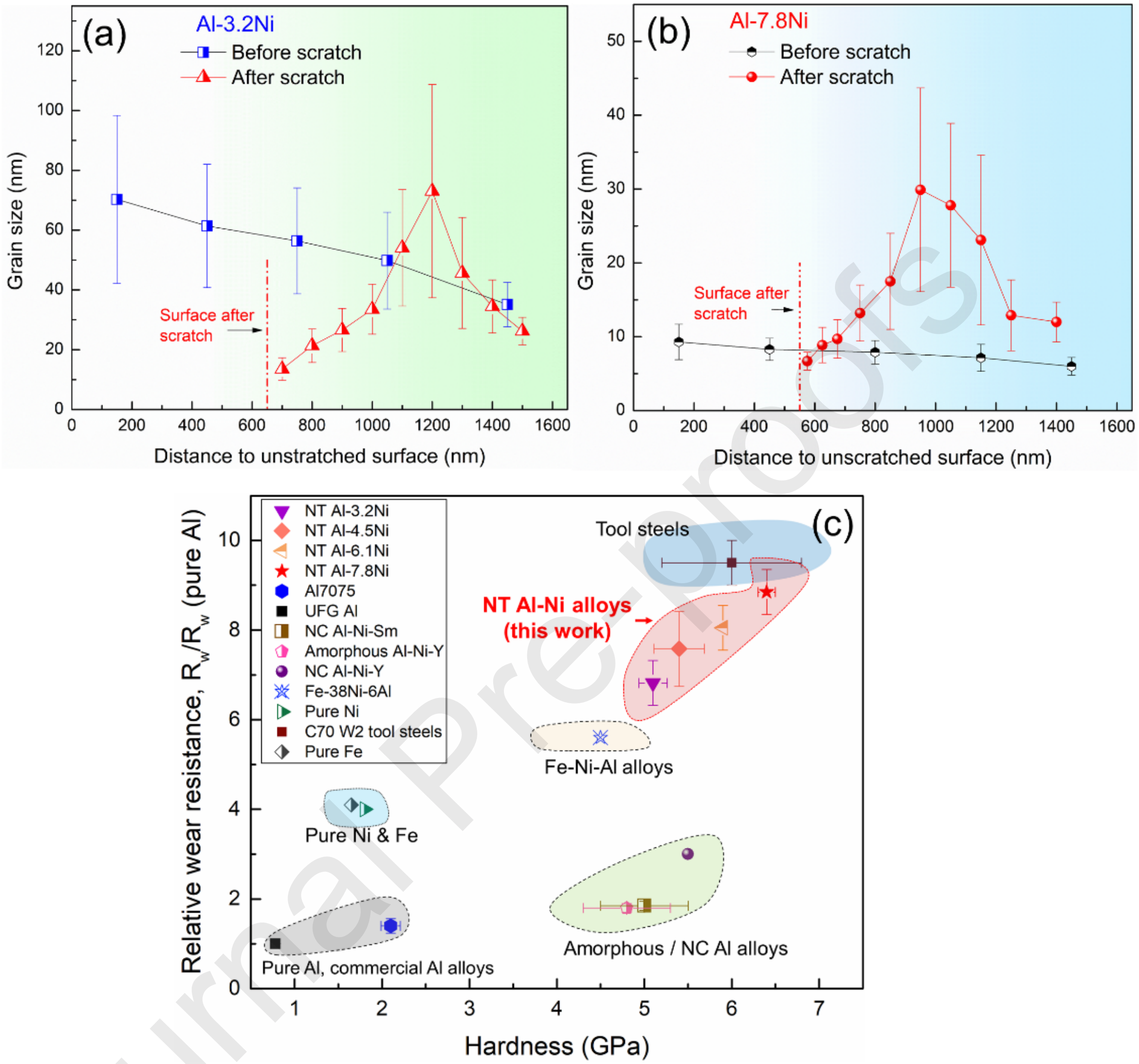

Figure 13. Grain size of (a) Al-3.2Ni and (b) Al-7.8Ni before and after scratch tests plotted as a function of distance to sample surface. (c) Comparison of relative wear resistances (Rw /Rw (pure Al)) between NT Al-Ni alloys and other metallic materials [38, 61, 65, 68-71].

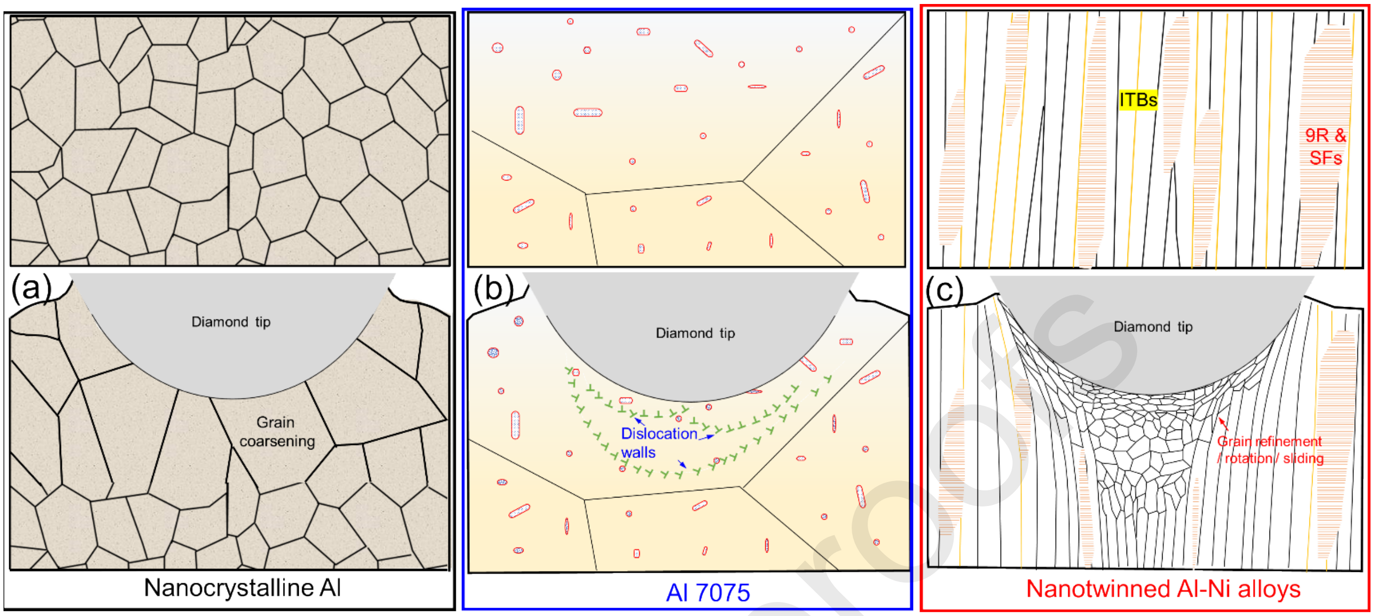

Figure 14. (a-c) Schematics showing the microstructure evolutions for the nanocrystalline Al, Al 7075 and nanotwinned Al-Ni alloys under the low-speed nanoscratch test.

Table 1. Physical properties of tested samples

Sample name	**Surface roughness (nm)**	**Hardness (H) (GPa)**	**Young's Modulus (E) (GPa)**	**(H/E)**	**Thickness (µm)**	**Grain size (nm)**
Al	5.63 ± 0.2	0.78 ± 0.03	69.3 ± 4	0.011	1.6	~500
Al7075 T6	18 ± 6	2.1 ± 0.112	70.2 ± 5	0.030	Bulk	~10000
Al-3.2Ni	2.8 ± 0.2	5.1 ± 0.16	109.7± 6	0.046	1.6	53 ±19
Al-4.5Ni	2.2 ± 0.1	5.4 ± 0.29	109.7 ± 4.5	0.049	1.6	39 ± 10
Al-6.1Ni	2.0 ± 0.28	5.9 ± 0.17	105.3 ± 9	0.056	1.6	14 ± 7
Al-7.8Ni	2.0 ± 0.5	6.4 ± 0.08	108.8 ± 3	0.059	1.6	7.8 ± 2

Table 2. The coefficient of friction (COF) at different loads

	5 mN	**10 mN**	**30mN**	**50mN**	**70mN**
Al	0.49± 0.03	0.52± 0.02	-	-	-
Al7075	0.25 ± 0.02	0.27± 0.02	0.45±0.02	0.61±0.027	0.70± 0.05
Al-3.2Ni	0.25± 0.01	0.23± 0.03	0.25±0.025	0.35±0.02	0.39± 0.02
Al-4.5Ni	0.2±0.06	0.21 ± 0.04	0.24±0.05	0.33±0.01	0.37± 0.05
Al-6.1Ni	0.25 ± 0.05	0.18± 0.02	0.24±0.04	0.31±0.02	0.37± 0.04
Al-7.8Ni	0.24 ± 0.05	0.20 ± 0.01	0.25 ± 0.02	0.31±0.02	0.38± 0.03

Table 3. **Calculated wear rates (1×10^{-3} $mm^3/(N\cdot m)$)**

	5 mN	**10 mN**	**30mN**	**50mN**	**70mN**
Al	65.3 ± 4.4	114.6 ± 3.4	163.6± 3.8	-	-
Al7075	33.7 ± 2.4	40.4± 2.2	72.1±4.4	131.3± 2.5	153.4± 3.0
Al-3.2Ni	7.5 ± 0.1	10.2± 0.1	17.0 ± 1.0	27.0±1.5	31.0±1.0
Al-4.5Ni	6.0 ± 0.1	8.7 ± 0.7	15.4 ± 1.0	22.7±1.0	27.3 ± 1.4
Al-6.1Ni	4.1 ± 0.7	5.1±0.7	15.0 ± 0.8	24.9±0.8	24.9±1.0
Al-7.8Ni	3.3 ± 0.3	5.3 ± 0.5	16.6 ± 10	21.1±0.7	23.6 ± 1.0

Table 4. Calculated Wear resistance, R_w (GPa) at different load ranges

	5-30 mN	**R-square**	**30-70 mN**	**R-square**	**5-70 mN**	**R-square**
Al	4.4 ± 0.1	0.99	-	-	4.4 ± 0.09	0.99
Al7075	12.1 ± 1.8	0.98	4.7 ± 0.1	0.999	6.1 ± 0.64	0.87
Al-3.2Ni	52.45 ± 3.2	0.99	24.0 ± 0.1	0.999	30.1 ± 2.0	0.97
Al-4.5Ni	56.1 ± 3.9	0.99	27.6 ± 0.2	0.997	33.8 ± 3.7	0.92
Al-6.1Ni	54.5 ± 8.0	0.92	30.4 ± 4.1	0.94	35.4 ± 2.0	0.97
Al-7.8Ni	51.4 ± 2.5	0.99	35.2 ± 0.5	0.999	39.0 ± 2.0	0.98

Table 5. Comparison of coefficient of friction (COF) of Al alloys collected by different methods [8,21,54–59]

Study	**Material**	**Testing method**	**Normal load (mN)**	**Tip geometry/dimension**	**COF**
Kang *et al.* (Appl. Surf. Sci. 2016)	3D printed Al-Si alloys	Sliding (ball on disc)	2000	Al_2O_3 ball / d = 6 mm	0.5±0.05
H.H. Kim *et al.* (MSE A 2008)	Al 6061alloys	Nanoscratch	10	Conical tip / r = 6 µm	0.31±0.05
V. Bhattacharya. *et al.* (Acta Mater. 2004)	Al with micro Pb	sliding (pin on disc)	490-40000	Steel pin / NA	0.4 ± 0.1
B. Venkataraman *et al.* (Wear 2000)	Al 7075 Al-40SiC Al	Sliding (pin on disc)	30000-220000	Pin / contact area = 28.3 mm^2	0.4 ± 0.05 0.68 ± 0.1 0.55-0.58
M. Tocci *et al.* (Metals, 2019)	3D printed AlSi10Mg	Sliding (pin on disc)	1000	Steel ball / d = 6 mm	0.42-0.5
Y. Wang *et. al*	Al	Nanoscratch	0-0.5	Berkovich tip	0.25-0.3

(Appl. Surf. Sci. 2019)					
J. Qu *et al.* (Wear ,2011)	Al6061-T6 Al6061 with Al_2O_3	Sliding (ball on disc)	25000	Steel ball / d = 9 mm	0.75-0.85 0.45-0.5
S.R. Bakshi *et al.* (Thin solid films,2010)	Al with carbon nanotubes (CNT)	Nanoscratch	1-3	Berkovich tip	0.2
J. S. S. Babu *et al.* (Met. Mater. Int. 2020)	A356 Al alloy with CNT and Al_2O_3	Nanoscratch	50-100	Berkovich tip	0.32-0.48
This work	Al7075	Nanoscratch	5-70	Conical tip / r = 5 µm	0.25-0.7
This work	**NT Al-Ni alloys**	**Nanoscratch**	**5-70**	**Conical tip** / r = 5 µm	**0.2-0.38**
This work	UFG Al	Nanoscratch	5-10	Conical tip / r = 5 µm	0.49-0.52

**d- diameter of tip; r-radius of tip*

Graphical abstract

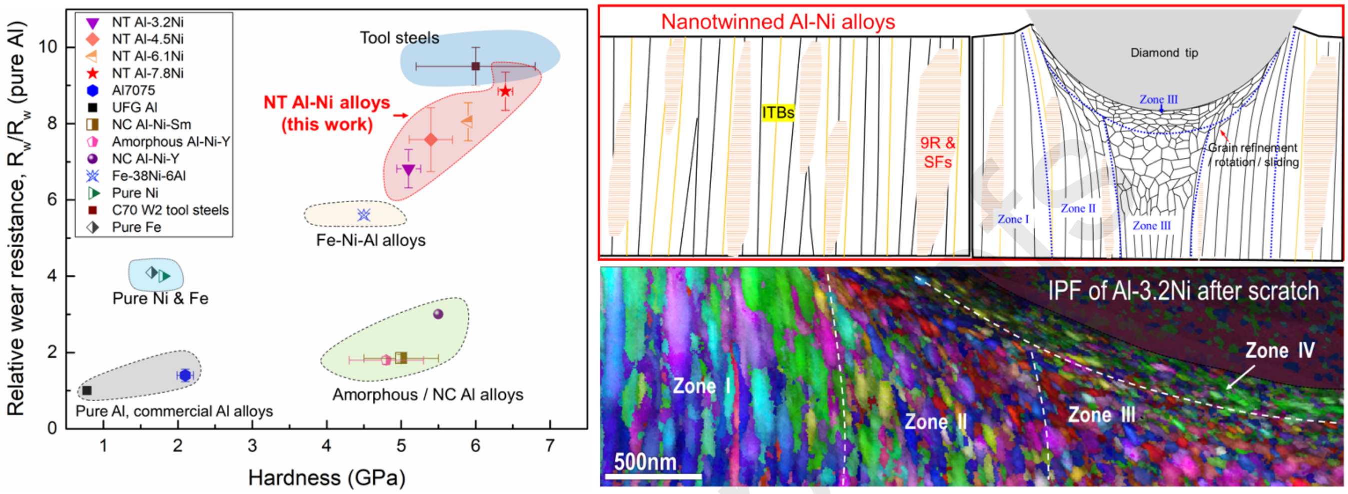

1. Tribological behaviors of ultrafine-grained Al, Al 7075 alloy, and nanotwinned Al–Ni alloys were investigated via nanoscratch.
2. Nanotwinned Al-Ni alloys exhibit superior tribological properties compared with Al and Al 7075 alloys.
3. Nanoscratch can generate the accumulation of dislocation walls and gradual grain reorientation in Al 7075.
4. Nanotwinned columnar grains in Al-Ni can evolve into equiaxed nanograins with gradient gain size during scratch.
5. The outstanding wear properties of nanotwinned Al–Ni alloys arise from their high strength and good work hardening capability.

Yifan Zhang conceived the idea, prepared the manuscript drafts, performed the scratch experiments, TEM and ASTAR characterizations and data analyses.

Tongjun Niu helped with the scratch tests, TEM and ASTAR analyses and manuscript revisions.

Nicholas A. Richter helped with TEM sample preparations and manuscript revisions.

Tianyi Sun prepared the samples for scratch tests and helped with ASTAR data analyses.

Nan Li helped with the scratch tests and manuscript revision .

Haiyan Wang supervised the TEM experiments and helped manuscript revisions.

Xinghang Zhang conceived the idea, revised manuscript, and supervised the whole project.

Declaration of interests

☒ The authors declare that they have no known competing financial interests or personal relationships that could have appeared to influence the work reported in this paper.

☐ The authors declare the following financial interests/personal relationships which may be considered as potential competing interests: